J. Fluid Mech. (2008), *vol.* 611, *pp.* 107–130. © 2008 Cambridge University Press
doi:10.1017/S002211200800267X Printed in the United Kingdom

Visualizing the geometry of state space in plane Couette flow

J. F. GIBSON, J. HALCROW AND P. CVITANOVIĆ

School of Physics, Georgia Institute of Technology, Atlanta, GA 30332, USA

(Received 9 August 2007 and in revised form 28 April 2008)

Motivated by recent experimental and numerical studies of coherent structures in wall-bounded shear flows, we initiate a systematic exploration of the hierarchy of unstable invariant solutions of the Navier–Stokes equations. We construct a dynamical 10^5-dimensional state-space representation of plane Couette flow at Reynolds number $Re = 400$ in a small periodic cell and offer a new method of visualizing invariant manifolds embedded in such high dimensions. We compute a new equilibrium solution of plane Couette flow and the leading eigenvalues and eigenfunctions of known equilibria at this Re and cell size. What emerges from global continuations of their unstable manifolds is a surprisingly elegant dynamical-systems visualization of moderate-Re turbulence. The invariant manifolds partially tessellate the region of state space explored by transiently turbulent dynamics with a rigid web of symmetry-induced heteroclinic connections.

1. Introduction

In a seminal paper, Hopf (1948) envisaged the function space of Navier–Stokes velocity fields as an infinite-dimensional state space, parameterized by viscosity, boundary conditions and external forces, in which each three-dimensional fluid velocity field is represented as a single point. Steady laminar states correspond to equilibria that are globally stable for sufficiently large viscosity. As the viscosity decreases (Reynolds number, Re, increases), turbulence sets in, represented by chaotic state-space trajectories. Hopf's observation that viscosity causes state-space volumes to contract under the action of dynamics led to his key conjecture: that long-term, typically observed solutions of the Navier–Stokes equations lie on finite-dimensional manifolds embedded in the infinite-dimensional state space of allowed velocity fields. These manifolds, known today as 'inertial manifolds', are well-studied in the mathematics of spatio-temporal PDEs. Their finite dimensionality for non-vanishing viscosity parameters has been rigorously established in certain settings by Foias *et al.* (1985) and collaborators.

Since Hopf's time, engineers and applied mathematicians have assembled a body of empirical evidence that moderately turbulent flows exhibit organized, intrinsically low-dimensional behaviour for a variety of conditions (see Holmes, Lumley & Berkooz 1996, Panton 1997 and Robinson 1991 for good overviews of this large body of work). The experiments of Kline *et al.* (1967), for example, revealed spatially organized streaks in the turbulent boundary layer. The numerical simulations of Kim, Moin & Moser (1987) opened access to the full three-dimensional velocity field of channel flows and paved the way for more detailed studies of organization in wall-bounded flows. The work of Hamilton, Kim & Waleffe

https://doi.org/10.1017/S002211200800267X Published online by Cambridge University Press

(1995) began a fruitful line of research; it identified from numerical simulations a remarkably well-defined quasi-cyclic process among streamwise streaks and vortices (or 'rolls') in low-Reynolds-number plane Couette flow. Waleffe (1995, 1997) further developed these ideas into a 'self-sustaining process theory' that explains the quasi-cyclic roll-streak behaviour in terms of the forced response of streaks to rolls, growth of streak instabilities, and nonlinear feedback from streak instabilities to rolls.

The preponderance of recurrent coherent states in wall-bounded shear flows suggests that their long-time dynamics lie on low-dimensional state-space attractors. This has motivated a number of workers to model such flows with low-dimensional dynamical systems. Aubry *et al.* (1988) (see also Holmes *et al.* 1996) used 'proper orthogonal decomposition' (POD) of experimental data and Galërkin projection of the Navier–Stokes equations to produce low-order models of coherent structures in boundary-layer turbulence. These models reproduce some qualitative features of the boundary layer, but their quantitative accuracy and the validity of simplifying assumptions in their derivation are uncertain (Zhou & Sirovich 1992; Sirovich & Zhou 1994; Gibson 2002). POD models for plane Couette flow were developed by Smith, Moehlis & Holmes (2005).

Another class of low-order models of plane Couette flow derives from the self-sustaining process discussed above (Dauchot & Vioujard 2000; Moehlis *et al.* 2004, 2005; Manneville 2004; Skufca 2005). These models use analytic basis functions explicitly designed to represent the streaks, rolls and instabilities of the self-sustaining process, compared to the numerical basis functions of the POD, which represent statistical features of the flow. They improve on the POD models by capturing the linear stability of the laminar flow and saddle-node bifurcations of non-trivial three-dimensional equilibria consisting of rolls, streaks and streak undulations. The work of Skufca, Yorke & Eckhardt (2006), based on a Schmiegel (1999) nine-variable model, offers an elegant dynamical systems picture, with the stable manifold of a periodic orbit defining the basin boundary that separates the turbulent and laminar attractors at $Re < 402$ and the stable set of a higher-dimensional chaotic object defining the boundary at higher Re. However, these models share with POD models a sensitive dependence on modelling assumptions and uncertain quantitative relations to fully resolved simulations. A systematic study of the convergence of POD/Galërkin models of plane Couette flow to fully resolved simulations indicates that dimensions typical in the literature (10–10^2) are orders of magnitude too low for either short-term quantitative prediction or reproduction of long-term statistics (Gibson 2002).

The lack of quantitative success in low-dimensional modelling motivates yet another approach: the calculation of exact invariant solutions of the fully resolved Navier–Stokes equations. The idea here is to bypass low-dimensional modelling and to treat fully resolved CFD algorithms directly as very high-dimensional dynamical systems. Nagata (1990) computed a 'lower-branch' and 'upper-branch' pair of non-trivial equilibrium solutions to plane Couette flow by continuation and bifurcation from a wavy vortex solution of Taylor–Couette flow. Starting with physical insights from the self-sustaining process, Waleffe (1998, 2001, 2003) generated, *ab initio*, families of exact three-dimensional equilibria and travelling waves of plane Couette and Poiseuille flows for a variety of boundary conditions and Re numbers, using a 10^4-dimensional Newton search and continuation from non-equilibrium states that approximately balanced the mechanisms highlighted by the self-sustained process. As noted in Waleffe (2003), these solutions, and Clever & Busse's (1992) equilibria of

https://doi.org/10.1017/S002211200800267X Published online by Cambridge University Press

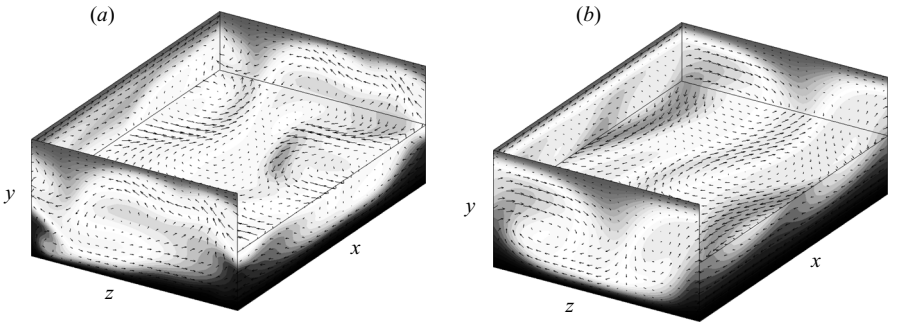


FIGURE 1. Snapshots of plane Couette turbulence at $Re = 400$. Total velocity fields (u, v, w) in a periodic cell of size $\Omega = [7\pi/4, 2, 6\pi/5]$ (Hamilton *et al.* 1995) are shown with arrows for in-plane velocity and greyscale for the streamwise velocity component u: light/dark grey indicates $u = \pm 1$; white, $u = 0$. The upper wall at $y = 1$ and the upper half of the fluid are cut away to show the velocity in the $y = 0$ midplane. The two snapshots shown are different instants from a simulation initiated with a random pertubation, selected to show (*a*) minimum and (*b*) maximum organization in the turbulent field. In particular, (*b*) resembles the upper-branch equilibrium shown in figure 3(*c*).

plane Couette flow with Rayleigh–Bénard convection, are homotopic to the Nagata equilibria under smooth transformations in the flow conditions. (We have confirmed that the upper-branch solutions of Nagata and Waleffe are the same by continuing Waleffe's solution to Nagata's cell size and Reynolds number and comparing plots of the velocity field to figure 8 of Nagata (1990).) Faisst & Eckhardt (2003) and Wedin & Kerswell (2004) carried the idea of a self-sustaining process over to pipe flow and applied Waleffe's continuation strategy to derive families of travelling-wave solutions for pipes. Travelling waves for plane Couette flow were computed by Nagata (1997) using a continuation method. Later, travelling waves for pressure-driven channel flow were obtained by Itano & Toh (2001) with a shooting method. The first short-period unstable periodic solutions of Navier–Stokes were computed by Kawahara & Kida (2001). Viswanath (2007) computed relative periodic orbits (orbits which repeat themselves with a translation) and further periodic orbits of plane Couette flow that exhibit breakup and reformation of roll–streak structures.

The exact solutions described above turn out to be remarkably similar in appearance to coherent structures observed in direct numerical simulation (DNS) and experiment. Waleffe (2001) coined the term 'exact coherent structures' to emphasize this connection. The upper-branch solution, for example, captures many statistical features of turbulent plane Couette flow and appears remarkably similar to the roll–streak structures observed in DNS (compare figure 1*b* to figure 3*c*). Waleffe (2003) showed that the upper and lower-branch equilibria appear at lowest Reynolds number with streak spacing of 100^+ wall units, an excellent match to that observed in Kline *et al.* (1967). The periodic orbits of Kawahara & Kida (2001) and Viswanath (2007) appear to be embedded in plane Couette flow's natural measure, and most of them capture basic statistics more closely than the equilibria (see figure 2). In pipe flow, high-speed streaks that match the travelling-wave solutions in cross-section have been observed in beautiful experiments using stereoscopic particle image velocimetry (Barenghi 2004; Busse 2004; Hof *et al.* 2004). Li & Graham (2007) found that the deformations of exact coherent solutions of plane Poiseuille flow caused by addition of viscoelasticity are very similar to experimentally observed changes in turbulent structures caused by

https://doi.org/10.1017/S002211200800267X Published online by Cambridge University Press

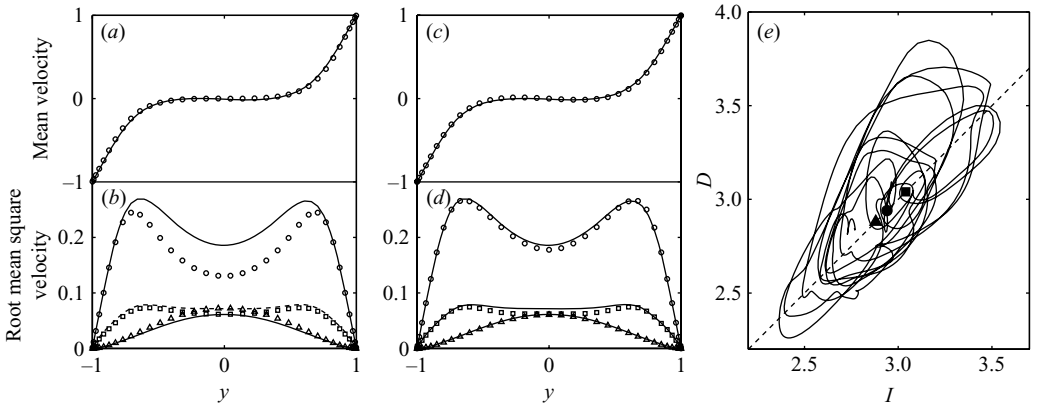


FIGURE 2. (a,b) Spatial-mean and spatial-r.m.s. total velocity profiles of the upper-branch equilibrium (symbols) in $\Omega = [2\pi/1.14, 2, 4\pi/5]$ against temporal mean and r.m.s. profiles for sustained turbulent DNS data in $[7\pi/4, 2, 6\pi/5]$ (lines). $Re = 400$ for both. (c,d) Temporal mean and r.m.s. velocity profiles for the $T = 87.89$ periodic orbit of Viswanath (2007) for $[7\pi/4, 2, 6\pi/5]$ and $Re = 400$ (symbols), against the same turbulent data shown in (a,c). In (a,c), mean values of u are marked with $\circ$; in (b,d) r.m.s. values of u, v, w are marked with $\circ, \triangle, \square$. (e) Wall-shear power input I versus viscous dissipation D for a typical trajectory of sustained turbulence in the $[7\pi/4, 2, 6\pi/5]$ cell (lines), mean dissipation rates of turbulent flow $\overline{D} = 2.88$ ($\blacktriangle$), the $T = 87.89$ periodic orbit $\overline{D} = 2.94$ ($\bullet$), and the upper-branch equilibrium $D_{UB} = 3.04$ ($\blacksquare$). The laminar equilibrium dissipation rate is $D = 1$ (not shown).

polymer additives. Additionally, there is preliminary evidence that the instabilities of these exact solutions play important dynamic roles. The relevance of steady solutions to sustained turbulence and transition to turbulence is discussed in Waleffe (2003), Jiménez *et al.* (2005) and Schneider, Eckhardt & Yorke (2007). The stable manifold of the lower-branch solution appears to control an important portion of the basin boundary between the turbulent and laminar attractors (Waleffe & Wang 2005; Wang, Gibson & Waleffe 2007; Viswanath 2008). Kerswell & Tutty's (2007) numerical simulations suggest that the unstable manifolds of lower-branch travelling waves act as similar boundaries in pipe flow, and that turbulent fields make occasional visits to the neighbourhoods of travelling waves.

Together, these results form a new way of thinking about coherent structures and turbulence: (a) that coherent structures are the physical images of the flow's least unstable invariant solutions, (b) that turbulent dynamics consists of a series of transitions between these states, and (c) that intrinsic low-dimensionality in turbulence results from the low number of unstable modes for each state (Waleffe 2002). The long-term goals of this work are to develop this vision into a quantitative predictive description of moderate-Re turbulence, and to use this description to control flows and explain their statistics. Much of this has already been accomplished in the simpler context of the Kuramoto–Sivashinsky equation (Christiansen, Cvitanović & Putkaradze 1997; Cvitanović, Davidchack & Siminos 2008).

In this paper, we take a few steps towards realizing these goals in the case of plane Couette flow in a small periodized cell. In § 2, we review the physical characteristics and symmetries of plane Couette flow. Section 3 discusses the computation of invariant solutions and their eigenvalues and presents (a) a new equilibrium solution of plane Couette and (b) the linear stability analysis of this and the Nagata lower- and upper-branch equilibria. These computations set the stage for the main advance reported

https://doi.org/10.1017/S002211200800267X Published online by Cambridge University Press

in this paper, visualization and exploration of the state space of moderate-Re plane Couette flow, undertaken in § 4. The combination of equilibrium solutions, linear stability analysis, and state-space portraiture reveals previously unseen dynamical connections among the invariant solutions of plane Couette flow. Particularly beautiful and unexpected are the discrete symmetry enforced interrelations between unstable manifolds manifest in figures 5–9.

2. Plane Couette flow

Plane Couette flow is comprised of an incompressible viscous fluid confined between two infinite parallel plates moving in-plane at constant velocities. We take the length scale L to be half the distance between the walls and the velocity scale U to be half the relative wall velocity. After non-dimensionalization and absorption of fluid density into the pressure field, the Navier–Stokes equations take the form

$$\frac{\partial \boldsymbol{u}}{\partial t} + \boldsymbol{u}\cdot\nabla\boldsymbol{u} = -\nabla p + \frac{1}{Re}\nabla^2\boldsymbol{u}\,, \quad \nabla\cdot\boldsymbol{u} = 0\,,$$

where the Reynolds number is defined as $Re = UL/\nu$ and ν is the kinematic viscosity of the fluid. The plates move at speed ± 1 along the 'streamwise' x-axis, the direction normal to the plates is the 'wall-normal' y-axis, $y \in [-1, +1]$, and the in-plane z-axis, normal to the plate velocity, is referred to as 'spanwise'. The x, y, z unit vectors are $\hat{\boldsymbol{x}}, \hat{\boldsymbol{y}}, \hat{\boldsymbol{z}}$. (We use boldface to indicate vectors in three spatial dimensions.) The velocity field $\boldsymbol{u}$ has streamwise, wall-normal and spanwise components $\boldsymbol{u} = [u, v, w]$; the velocity at point $\boldsymbol{x}$ and time t is $\boldsymbol{u}(\boldsymbol{x}, t) = [u, v, w](x, y, z, t)$. The no-slip boundary conditions at the walls are $\boldsymbol{u}(x, \pm 1, z) = [\pm 1, 0, 0]$. As a simplifying assumption, we replace the infinite x and z directions with a periodic cell of lengths L_x and L_z, or equivalently, the fundamental wavenumbers $\alpha = 2\pi/L_x$ and $\gamma = 2\pi/L_z$. We denote the periodic domain of the cell by $\Omega = [0, L_x] \times [-1, 1] \times [0, L_z]$ or simply $\Omega = [L_x, 2, L_z]$. We assume that the spatial mean of the pressure gradient is zero, i.e. there is no pressure drop across the cell in x or z.

Replacing $\boldsymbol{u}$ with $\boldsymbol{u} + y\,\hat{\boldsymbol{x}}$ recasts Navier–Stokes in terms of the difference of the velocity from laminar flow:

$$\frac{\partial \boldsymbol{u}}{\partial t} + y\frac{\partial \boldsymbol{u}}{\partial x} + v\,\hat{\boldsymbol{x}} + \boldsymbol{u}\cdot\nabla\boldsymbol{u} = -\nabla p + \frac{1}{Re}\nabla^2\boldsymbol{u}\,, \quad \nabla\cdot\boldsymbol{u} = 0\,. \tag{2.1}$$

The difference $\boldsymbol{u}$ satisfies Dirichlet conditions at the walls, $\boldsymbol{u}(x, \pm 1, z) = 0$. Hereinafter, we refer to the difference $\boldsymbol{u}$ as 'velocity' and $\boldsymbol{u} + y\,\hat{\boldsymbol{x}}$ as 'total velocity', and we take (2.1) as the Navier–Stokes equations for plane Couette flow.

Plane Couette flow is the simplest of all shear flows, and it is here that roll–streak structures take their simplest form. For moderate values of Re, the rolls span the full distance between the walls, whereas in channel and boundary-layer flows such structures are bounded by a wall on one side and open flow on the other. Figure 1 shows two typical velocity fields from a simulation in the 'HKW' cell $\Omega = [7\pi/4, 2, 6\pi/5]$ at $Re = 400$. The numerical simulations of Hamilton *et al.* (1995) indicate that this is roughly the smallest cell and Reynolds number that sustains turbulence for long time scales. Roll–streak structures are evident, particularly in figure 1(*b*). The rolls circulate high-speed fluid towards the walls and low-speed flow away (where velocity is relative to either wall); the resulting streaks of high-speed fluid near the walls dramatically increase drag compared to laminar flow. For example, the power input required to maintain constant wall velocity in plane Couette flow

https://doi.org/10.1017/S002211200800267X Published online by Cambridge University Press

increases by a factor of three if the flow goes turbulent (see figure 2*e*). The practical importance of roll–streak dynamics derives from their role in momentum transfer and turbulent energy production and their generic occurrence in wall-bounded shear flows.

Except for figure 1 and parts of figure 2, the results in this paper are for $Re = 400$ and $\Omega = [2\pi/1.14, 2, 4\pi/5]$, first studied in Waleffe (2002). This cell matches the HKW cell $[7\pi/4, 2, 6\pi/5]$ closely in x ($7/4 \approx 2/1.14$). The z length scale $L_z = 4\pi/5$ was chosen as a compromise between $L_z = 6\pi/5$ of the HKW cell (which sustains turbulence for long time scales, but has equilibria only with doubled period in z) and its first harmonic $L_z = 3\pi/5$ (which has equilibria at the fundamental harmonic, but tends to decay to laminar flow). Simulations for these parameters tend to decay to the laminar state within several hundred non-dimensionalized time units L/U, but the transient dynamics serves well to illustrate our invariant manifolds construction. Whether a given cell size sustains turbulence indefinitely is a subtle dynamical issue: Schmiegel & Eckhardt (1997) and Schmiegel (1999) observe only chaotic transients in their studies.

2.1. *Energy transfer rates*

The kinetic energy density E, the bulk viscous dissipation rate D, and the wall-shear power input I of the total velocity field of plane Couette flow are given by

$$E(t) = \frac{1}{V}\int_\Omega \mathrm{d}\boldsymbol{x}\ \tfrac{1}{2}|\boldsymbol{u} + y\,\hat{\boldsymbol{x}}|^2, \tag{2.2}$$

$$D(t) = \frac{1}{V}\int_\Omega \mathrm{d}\boldsymbol{x}\ |\nabla \times (\boldsymbol{u} + y\,\hat{\boldsymbol{x}})|^2, \tag{2.3}$$

$$I(t) = 1 + \frac{1}{2A}\int_A \mathrm{d}x\,\mathrm{d}z\ \left(\left.\frac{\partial u}{\partial y}\right|_{y=1} + \left.\frac{\partial u}{\partial y}\right|_{y=-1}\right), \tag{2.4}$$

where $V = 2L_xL_z$ and $A = L_xL_z$. The normalizations are chosen so that $D = I = 1$ for laminar flow and $\dot{E} = I - D$. Figure 2(*e*) shows I *vs.* D for a turbulent trajectory and several invariant solutions. Equilibria and relative equilibria must fall on the line $I = D$ where these two quantities are in balance. The energy input and dissipation rates must also balance in averages over a single period of a periodic orbit or relative periodic orbit p,

$$D_p = 1/T_p \int_0^{T_p} \mathrm{d}t\ D(t) = 1/T_p \int_0^{T_p} \mathrm{d}t\ I(t) = I_p,$$

as well as for long-term averages, $\overline{I(t)} = \overline{D(t)}$.

We note that the turbulent trajectory in figure 2 stays clear of the much lower dissipation rates $D_{LB} = 1.43$ and $D_{NB} = 1.45$ of the equilibrium solutions $\boldsymbol{u}_{LB}$ and $\boldsymbol{u}_{NB}$ (see § 3.2), so these equilibria are far from the turbulent attractor. The energy, the dissipation rate, and mean and r.m.s. velocity profiles of the Nagata (1990) upper-branch equilibrium and most of the periodic orbits of Kawahara & Kida (2001) and Viswanath (2007) are numerically close to the long-term turbulent averages. This suggests that the solutions play an important role in turbulent dynamics, but turbulent statistics do not simply follow from the properties of a few solutions. On the contrary, periodic orbit theory shows that the statistics of dynamical systems are given by sums over hierarchies of periodic orbits, with weights determined by the orbits' lengths and stabilities (Cvitanović *et al.* 2007).

https://doi.org/10.1017/S002211200800267X Published online by Cambridge University Press

2.2. *Symmetries*

Plane Couette flow is invariant under two discrete symmetries σ_1, σ_2 and a continuous two-parameter group of translations $\tau(\ell_x, \ell_z)$:

$$\sigma_1\,[u, v, w](x, y, z) = [u, v, -w](x, y, -z), \tag{2.5a}$$

$$\sigma_2\,[u, v, w](x, y, z) = [-u, -v, w](-x, -y, z), \tag{2.5b}$$

$$\tau(\ell_x, \ell_z)[u, v, w](x, y, z) = [u, v, w](x + \ell_x, y, z + \ell_z). \tag{2.5c}$$

The Navier–Stokes equations and boundary conditions are invariant under any symmetry s in the group generated by these symmetries: $\partial(s\boldsymbol{u})/\partial t = s(\partial \boldsymbol{u}/\partial t)$.

The Nagata (1990) lower- and upper-branch equilibria (hereinafter referred to as $\boldsymbol{u}_{LB}$ and $\boldsymbol{u}_{UB}$) are invariant under the action of the subgroup $S = \{1, s_1, s_2, s_3\}$, where $s_1 = \tau(L_x/2, 0)\,\sigma_1$, $s_2 = \tau(L_x/2, L_z/2)\,\sigma_2$ and $s_3 = s_1 s_2$. That is, $s\,\boldsymbol{u}_{LB} = \boldsymbol{u}_{LB}$ and $s\,\boldsymbol{u}_{UB} = \boldsymbol{u}_{UB}$ for $s \in S$. The s_1 and s_2 symmetries are often called the 'shift-reflect' and 'shift-rotate' symmetries. The group actions on velocity fields $\boldsymbol{u}$ are given by

$$s_1\,[u, v, w](x, y, z) = [u, v, -w]\big(x + \tfrac{1}{2}L_x,\ y,\ -z\big), \tag{2.6a}$$

$$s_2\,[u, v, w](x, y, z) = [-u, -v, w]\big(-x + \tfrac{1}{2}L_x,\ -y,\ z + \tfrac{1}{2}L_z\big), \tag{2.6b}$$

$$s_3\,[u, v, w](x, y, z) = [-u, -v, -w]\big(-x,\ -y,\ -z + \tfrac{1}{2}L_z\big). \tag{2.6c}$$

In a rough sense, this subgroup is important to plane Couette dynamics because combining half-cell shifts with σ_1 and σ_2 allows the largest and thus least dissipative structures possible in the given periodic cell.

We denote the space of velocity fields that satisfy the kinematic conditions of plane Couette flow by

$$\mathbb{U} = \{\boldsymbol{u} \mid \boldsymbol{\nabla}\cdot\boldsymbol{u} = 0,\ \boldsymbol{u}(x, \pm 1, z) = 0,\ \boldsymbol{u}(x, y, z) = \boldsymbol{u}(x + L_x, y, z) = \boldsymbol{u}(x, y, z + L_z)\}, \tag{2.7}$$

and the S-invariant subspace (Golubitsky & Stewart (2002)) of $\mathbb{U}$ by

$$\mathbb{U}_S = \{\boldsymbol{u} \in \mathbb{U} \mid s_j\boldsymbol{u} = \boldsymbol{u}\,,\ \ s_j \in S\}. \tag{2.8}$$

$\mathbb{U}_S$ is a dynamically invariant subspace of $\mathbb{U}$ since S symmetry is preserved by evolution under the Navier–Stokes equations.

A second important subgroup is the group of half-cell translations $T = \{1, \tau_x, \tau_z, \tau_{xz}\}$, where $\tau_x = \tau(L_x/2, 0)$, $\tau_z = \tau(0, L_z/2)$, and $\tau_{xz} = \tau_x\tau_z$. In general, the continuous translation $\tau(\ell_x, \ell_z)$ maps each state $\boldsymbol{u}$ into a 2-torus of dynamically equivalent states, and the group $\{1, \sigma_1, \sigma_2, \sigma_1\sigma_2\}$ maps these into four dynamically equivalent 2-tori. For $\boldsymbol{u} \in \mathbb{U}_S$, these four tori coincide, and this single torus intersects $\mathbb{U}_S$ at the four points $\tau\boldsymbol{u}$, $\tau \in T$. (Since elements of T commute with those of S, $\boldsymbol{u} \in \mathbb{U}_S$ implies $\tau\boldsymbol{u} \in \mathbb{U}_S$ for $\tau \in T$.) For example, the upper-branch equilibrium $\boldsymbol{u}_{UB}$ appears within $\mathbb{U}_S$ in four distinct half-cell translations, namely $\boldsymbol{u}_{UB}$, $\tau_x\boldsymbol{u}_{UB}$, $\tau_z\boldsymbol{u}_{UB}$, and $\tau_{xz}\boldsymbol{u}_{UB}$. In effect, restriction to the $\mathbb{U}_S$ subspace simplifies analysis of plane Couette dynamics by reducing the dynamical equivalence class of each velocity field from a set of four two-tori to a set of four points. In what follows we focus mostly on dynamics within $\mathbb{U}_S$.

https://doi.org/10.1017/S002211200800267X Published online by Cambridge University Press

3. Invariant solutions of plane Couette

Let $\boldsymbol{F}(\boldsymbol{u})$ represent the Navier–Stokes equation (2.1) for $\boldsymbol{u} \in \mathbb{U}$ (2.7) and $\boldsymbol{f}^t$ its time-t forward map

$$\frac{\partial \boldsymbol{u}}{\partial t} = \boldsymbol{F}(\boldsymbol{u}), \qquad \boldsymbol{f}^t(\boldsymbol{u}) = \boldsymbol{u} + \int_0^t \mathrm{d}\tau\, \boldsymbol{F}(\boldsymbol{u}). \tag{3.1}$$

$\boldsymbol{F}(\boldsymbol{u})$ admits of invariant solutions of the following types:

$$\boldsymbol{F}(\boldsymbol{u}_{EQ}) = 0 \qquad \text{equilibrium or steady state } \boldsymbol{u}_{EQ}, \tag{3.2a}$$

$$\boldsymbol{F}(\boldsymbol{u}_{TW}) = -\boldsymbol{c}\cdot\nabla\boldsymbol{u}_{TW} \qquad \text{relative equilibrium or travelling wave } \boldsymbol{u}_{TW},\ \text{velocity } \boldsymbol{c}, \tag{3.2b}$$

$$\boldsymbol{f}^{T_p}(\boldsymbol{u}_p) = \boldsymbol{u}_p \qquad \text{periodic orbit } p \text{ of period } T_p, \tag{3.2c}$$

$$\boldsymbol{f}^{T_p}(\boldsymbol{u}_p) = s_p\,\boldsymbol{u}_p \qquad \text{relative periodic orbit, period } T_p,\ \text{symmetry } s_p. \tag{3.2d}$$

Relative equilibria are allowed due to the continuous translation symmetry $\tau(\ell_x, \ell_z)$; boundary conditions require $\boldsymbol{c}\cdot\hat{\boldsymbol{y}} = 0$. The symmetry s_p for a relative periodic orbit is an element of the group generated by (2.5). We expect to see many more relative periodic orbits than periodic orbits because a trajectory that starts on and returns to a given torus is unlikely to intersect it at the initial point, unless forced to do so by a discrete symmetry. This indeed is the case for other PDEs with continuous symmetries, such as the complex Ginzburg–Landau equation (López *et al.* 2006) and the Kuramoto–Sivashinsky equation (Cvitanović *et al.* 2008). Restriction to the S-invariant subspace $\mathbb{U}_S$ defined in (2.8) eliminates relative equilibria and restricts relative periodic orbits to those with $s_p = \tau \in T$, the group of half-cell translations. After $2T_p$, these relative orbits will close to form true periodic orbits.

3.1. *Finite representation*

Computing the exact solutions and stability modes of plane Couette flow requires a finite, but fully resolved, discretization of the constrained partial differential and integral equations represented by (3.1) and (3.2). We investigated two approaches to discrete representation. In the first approach, the vector $u \in \mathbb{R}^d$ was formed by breaking the complex spectral expansion coefficients of a CFD algorithm into real and imaginary parts and then selecting from these a set of linearly independent real-valued variables. Our CFD algorithm, `channelflow.org`, is based on the velocity–pressure algorithm of Kleiser & Schumann (1980) with expansions

$$\boldsymbol{u}(\boldsymbol{x}, t) = \sum_{j=-J}^{J} \sum_{k=-K}^{K} \sum_{\ell=0}^{L} \sum_{m=1}^{3} \hat{u}_{jklm}\, T_\ell(y)\, \mathrm{e}^{2\pi\mathrm{i}(jx/L_x + kz/L_z)}\, \hat{\boldsymbol{x}}_m, \tag{3.3}$$

where the T_ℓ are Chebyshev polynomials and $(\hat{\boldsymbol{x}}_1, \hat{\boldsymbol{x}}_2, \hat{\boldsymbol{x}}_3) = (\hat{\boldsymbol{x}}, \hat{\boldsymbol{y}}, \hat{\boldsymbol{z}})$ unit vectors. The algorithm employs a Chebyshev tau method and tau correction for enforcement of incompressibility and boundary conditions. Computations in this paper used third-order semi-implicit backwards-differentiation time-stepping, dealiasing in the x, z transforms, and rotational calculation of the nonlinear advection term. The expansion (3.3) retains a number of linearly dependent terms, due to complex symmetries and the run-time enforcement of the incompressibility and boundary conditions. Intimate knowledge of the CFD algorithm and careful accounting is required to determine the precise number of linearly independent coefficients and a self-consistent method of converting back and forth between the state-space vector u and the expansion coefficients of $\boldsymbol{u}$. For our CFD algorithm and an $N_x \times N_y \times N_z$ grid,

https://doi.org/10.1017/S002211200800267X Published online by Cambridge University Press

d is slightly less than $2N_x(N_y-2)N_z$. The accounting for velocity–vorticity algorithms is somewhat simpler since incompressibility is eliminated at the outset. For further technical details, please refer to Viswanath (2007), Halcrow (2008), and documented codes at `channelflow.org`, or contact the authors.

In the second approach, we explicitly constructed a set of orthonormal divergence-free no-slip basis functions $\boldsymbol{\Phi}_n(\boldsymbol{x})$ and formed the state-space vector u from the coefficients $\hat{u}_n$ of the expansion $\boldsymbol{u}(\boldsymbol{x}) = \sum_{n=1}^{d} \hat{u}_n \boldsymbol{\Phi}_n(\boldsymbol{x})$. This approach produces a mathematically simpler representation, in that (i) all constraints are subsumed into the basis and eliminated from further consideration, (ii) an explicit ODE of the form $\dot{u} = F(u)$ and quadratic in the coefficients $\hat{u}_n$ can be derived via Galërkin projection of Navier–Stokes, and (iii) with proper normalization of the basis functions, the L^2 norm of the state-space vector $u \in \mathbb{R}^d$ is the same as the L^2 energy norm of the velocity field $\boldsymbol{u}$. The downside is that the formulation of the basis set is complicated, and it requires extra computation for orthogonalization and transforms between state-space vectors and the CFD representation. We found no practical advantages to the orthonormal basis. The results reported here were computed using CFD expansion coefficients for the state-space vector u.

The choice of discretization $u \in \mathbb{R}^d$ and CFD algorithm implicity defines a d-dimensional dynamical system $\dot{u} = F(u)$. Viswanath (2007) showed that invariant solutions and linear stability of F can be computed efficiently with Krylov subspace methods and numerical evaluation of the finite-time map $f^T : u(t) \to u(t+T)$ with the CFD algorithm. Equilibria may be computed as solutions of $f^t(u) - u = 0$ for fixed t; and periodic orbits as solutions of the same equation with varying t. Viswanath's algorithm for computing these solutions involves a novel combination of Newton descent, GMRES solution of the Newton equations, and 'trust-region' limitation to the magnitude of the Newton steps. The results reported in this paper, however, used a straight Newton-GMRES search, with no trust region modification. We will often discuss equilibria and linear stability in terms of the flow F, with the understanding that the computations are performed using the finite-time map f^T.

3.2. *Equilibria*

The starting points of our exploration of plane Couette state space are the Nagata (1990) and Waleffe (2003) $\boldsymbol{u}_{UB}$ and $\boldsymbol{u}_{LB}$ equilibrium solutions of plane Couette flow for $Re = 400$ and $[L_x, L_y, L_z] = [2\pi/1.14, 2, 4\pi/5]$, provided in numerical form by Waleffe. These fields employed an elliptical truncation of spectral coefficients (requiring $j^2/J^2 + k^2/K^2 + l^2/L^2 \leqslant 1$ for expansions of the form (3.3)) on a $32 \times 34 \times 32$ grid. We use Viswanath's Newton-GMRES algorithm to increase the resolution to a rectangular truncation ($|j| \leqslant J, |k| \leqslant K, l \leqslant L$) on a $32 \times 35 \times 32$ grid. The dimensionality of this finite representation is $d = 61\,506$. These recomputed solutions satisfy (3.2)

$$F(u) = 0\,, \qquad u = f^t(u) \tag{3.4}$$

in discrete form. At this spectral resolution, the Newton-GMRES search can reduce the residual of the discrete equilibrium equation to 10^{-14}, but the truncated coefficients are of the order of 10^{-6}, and the residual increases to the same level when the given solution is integrated at higher resolution. The accuracy of the equilibrium solutions is thus roughly single-precision.

Figure 3 shows the $\boldsymbol{u}_{LB}$ and $\boldsymbol{u}_{UB}$ equilibria as velocity fields, along with a third equilibrium $\boldsymbol{u}_{NB}$('N' for 'new') that was discovered in the course of this investigation. This equilibrium was found by initiating Newton-GMRES searches for solutions of the equilibrium equations from points within the unstable manifolds of $\boldsymbol{u}_{LB}$ and

https://doi.org/10.1017/S002211200800267X Published online by Cambridge University Press

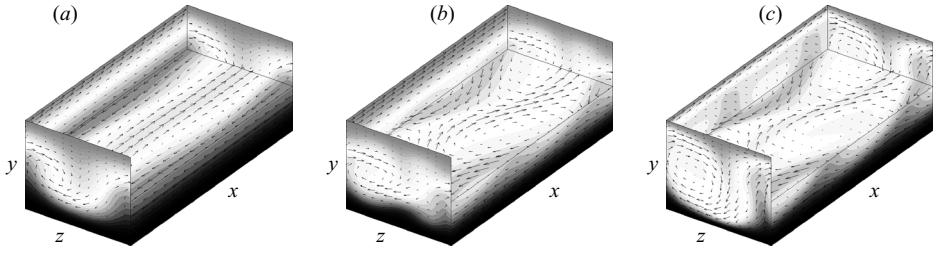


FIGURE 3. Equilibrium solutions of plane Couette flow. Total velocity fields of (*a*) $\boldsymbol{u}_{LB}$, the lower-branch equilibrium, (*b*) $\boldsymbol{u}_{NB}$, the 'new' equilibrium, and (*c*) $\boldsymbol{u}_{UB}$, the upper-branch equilibrium. $[L_x, L_y, L_z] = [2\pi/1.14, 2, 4\pi/5]$ and $Re = 400$. The plotting conventions are the same as in figure 1.

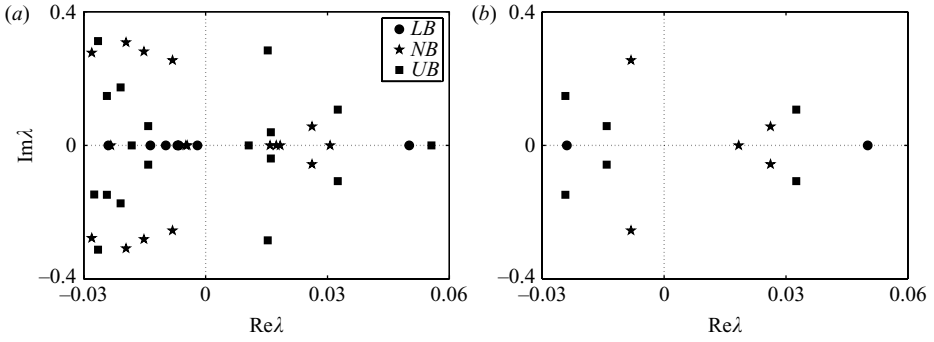


FIGURE 4. Leading $\boldsymbol{u}_{LB}$, $\boldsymbol{u}_{NB}$, $\boldsymbol{u}_{UB}$ eigenvalues in (*a*) the full space $\mathbb{U}$ (*b*) the S-invariant subspace $\mathbb{U}_S$. Numerical values are given in tables 1 and 2.

$\boldsymbol{u}_{UB}$ (see § 4). A portion of the one-dimensional unstable manifold of $\boldsymbol{u}_{LB}$, shown in figure 5, appears to be strongly influenced by a complex unstable eigenvalue of $\boldsymbol{u}_{NB}$. Initial guesses along this portion of the $\boldsymbol{u}_{LB}$ unstable manifold converge rapidly to $\boldsymbol{u}_{NB}$, to several digits of accuracy in a few Newton steps.

3.3. *Linear stability of equilibria*

Dynamics in the neighbourhood of an equilibrium solution are governed by the linear stability matrix

$$[DF]_{mn} = \frac{\partial F_m}{\partial u_n}. \tag{3.5}$$

Figure 4 shows the leading (most unstable) eigenvalues of $\boldsymbol{u}_{LB}$, $\boldsymbol{u}_{NB}$ and $\boldsymbol{u}_{UB}$, computed with Arnoldi iteration (Viswanath 2007). Figure 4(*a*) shows all computed eigenvalues; figure 4(*b*) shows those within the S-invariant subspace $\mathbb{U}_S$. The eigenfunctions $\boldsymbol{v}$ of DF at the equilibria are either symmetric, $s\boldsymbol{v} = \boldsymbol{v}$, or antisymmetric, $s\boldsymbol{v} = -\boldsymbol{v}$ for $s \in S$, since $s^2 = 1$. Thus, in general, the dynamics carries small perturbations of these equilibria into the full space $\mathbb{U}$. The $\boldsymbol{u}_{LB}$ equilibrium has a single unstable eigenvalue (Wang *et al.* 2007). Within $\mathbb{U}_S$, the u_{UB} equilibrium has a single unstable complex pair, and $\boldsymbol{u}_{NB}$ has one unstable real eigenvalue and one unstable complex pair.

The Arnoldi eigenvalues are accurate to 10^{-6}, as determined by repeated calculations with different random initial vectors and comparison of Arnoldi computations to analytically known eigenvalues of the laminar equilibrium. This

https://doi.org/10.1017/S002211200800267X Published online by Cambridge University Press

level of accuracy results from the use of off-centre finite differencing to estimate differentials of the flow in the Arnoldi iteration: $Df^t|_u v = (f^t(u+\epsilon v) - f^t(u))/\epsilon + O(\epsilon)$, with $\epsilon = 10^{-7}$. Tables of numerical eigenvalues and their symmetries are given in the Appendix (tables 1 and 2) and at `channelflow.org`.

3.4. *Linearized evolution*

Let λ, v_{EQ} be an eigenvalue, eigenvector solution of $DF|_{u_{EQ}} v = \lambda v$ at the equilibrium u_{EQ}. (We indicate particular invariant solutions with subscripts, such as u_{LB} or $\boldsymbol{u}_{LB}$ for the lower-branch equilibrium solution. The nth eigenvalue is $\lambda^{(n)}$, $n = 1, 2, \ldots$, in order of decreasing real part. Whenever the context allows it, we shall omit the eigenvalue and/or solution labels.) Then the linearized state-space dynamics $\dot{v} = DF|_{u_{EQ}} v$ about u_{EQ} has solution $v(t) = \mathrm{e}^{\lambda t} v_{EQ}$, and the initial condition $u(0) = u_{EQ} + \epsilon\, v_{EQ}$ with $\epsilon |v_{EQ}| \ll 1$ evolves as

$$u(t) = u_{EQ} + \epsilon\, v_{EQ}\, \mathrm{e}^{\lambda t} + O(\epsilon^2)\,. \tag{3.6}$$

The linearized evolution of the velocity field $\boldsymbol{u}(\boldsymbol{x}, t)$ can be derived by reconstructing the velocity fields from the corresponding state-space vectors, as discussed in § 3.1. Small perturbations about $\boldsymbol{u}_{EQ}$ along the eigenfunction $\boldsymbol{v}_{EQ}$ evolve as

$$\boldsymbol{u}(\boldsymbol{x}, t) = \boldsymbol{u}_{EQ}(\boldsymbol{x}) + \epsilon\, \boldsymbol{v}_{EQ}(\boldsymbol{x})\, \mathrm{e}^{\lambda t} + O(\epsilon^2)\,. \tag{3.7}$$

Complex eigenvalues and eigenvectors must be recast in real-valued form prior to conversion to velocity fields, since each element of the state-space vector v is the real or imaginary part of a complex-valued spectral coefficient in a CFD expansion such as (3.3). Let $\lambda_{EQ}^{(n,n+1)} = \mu^{(n)} \pm \mathrm{i}\omega^{(n)}$ be a complex eigenvalue pair and $v_{EQ}^{(n,n+1)} = v_r^{(n)} \pm \mathrm{i} v_i^{(n)}$ the corresponding complex eigenvectors. Then (dropping superscripts) the initial condition $u(0) = u_{EQ} + \epsilon\, v_r$ evolves as a real-valued spiral

$$u(t) = u_{EQ} + \epsilon\, (v_r \cos\omega t - v_i \sin\omega t)\, \mathrm{e}^{\mu t} + O(\epsilon^2)\,. \tag{3.8}$$

Real-valued fields $\boldsymbol{v}_r$ and $\boldsymbol{v}_i$ can be reconstructed from the real-valued vectors v_r and v_i, and the real-valued initial velocity field $\boldsymbol{u}(0) = \boldsymbol{u}_{EQ} + \epsilon\, \boldsymbol{v}_r$ evolves as

$$\boldsymbol{u}(t) = \boldsymbol{u}_{EQ} + \epsilon\, (\boldsymbol{v}_r \cos\omega t - \boldsymbol{v}_i \sin\omega t)\, \mathrm{e}^{\mu t} + O(\epsilon^2)\,. \tag{3.9}$$

3.5. *Unstable manifolds*

Let W_{EQ}^s (W_{EQ}^u) denote the stable (unstable) manifold of equilibrium $\boldsymbol{u}_{EQ}$. For each real-valued unstable eigenvalue $\lambda^{(n)}$, we shall refer to the orbit of an infinitesimal perturbation of $\boldsymbol{u}_{EQ}$ along the corresponding eigenfunction $\boldsymbol{v}_{EQ}^{(n)}$ as $W_{EQ}^{u(n)}$. This part of the $\boldsymbol{u}_{EQ}$ unstable manifold is one-dimensional and can be computed by DNS integration of the initial conditions $\boldsymbol{u}_{EQ} \pm \epsilon\, \boldsymbol{v}_{EQ}^{(n)}$, where $\epsilon \ll 1$.

For an unstable complex pair $\lambda^{(n,n+1)}$ of equilibrium $\boldsymbol{u}_{EQ}$, let $W_{EQ}^{u(n,n+1)}$ denote the orbit of a circle of infinitesimal radius in the plane about $\boldsymbol{u}_{EQ}$ spanned by $\boldsymbol{v}_r^{(n)}$, $\boldsymbol{v}_i^{(n)}$. This part of the $\boldsymbol{u}_{EQ}$ unstable manifold is two-dimensional; its shape can be traced out by computing a set of trajectories with initial conditions $\boldsymbol{u}_{EQ} + \epsilon(\boldsymbol{v}_r^{(n)} \cos\theta + \boldsymbol{v}_i^{(n)} \sin\theta)$ for a set of values of θ. In practice, we obtain a more uniform distribution of trajectories by setting initial conditions along the line $\boldsymbol{u}_{EQ} + \epsilon\, \boldsymbol{v}_r^{(n)}$, for a set of values of ϵ.

The global unstable manifolds $W_{EQ}^{u(n)}$ and $W_{EQ}^{u(n,n+1)}$ are invariant sets that preserve the symmetries shared by the equilibrium and the eigenvectors from which they are generated. The S-invariant subspace portions of the unstable manifolds of $\boldsymbol{u}_{LB}$, $\boldsymbol{u}_{UB}$ and $\boldsymbol{u}_{NB}$ have dimensionality of 1, 2 and 3, respectively (see figure 4*b*). In what follows, we will focus on these low-dimensional unstable manifolds confined to the $\mathbb{U}_S$ subspace.

https://doi.org/10.1017/S002211200800267X Published online by Cambridge University Press

4. The geometry of plane Couette state space

We now turn to the main theme of this paper: *exact state-space portraiture* of plane Couette flow dynamics. The state-space portraits are *dynamically intrinsic*, since the projections are defined in terms of solutions of the equations of motion, and *representation independent*, since the projection operation (the inner product (4.1)) is independent of the numerical representation. The method is by no means restricted to plane Couette flow or our choice of state-space representation or CFD algorithm. It can be applied to any high-dimensional dissipative flow, for example the Kuramoto–Sivashinsky flow (Cvitanović *et al.* 2008). Production of state-space portraits requires numerical data of three-dimensional velocity fields evolving in time (obtained from simulation or experiment), estimates of important physical states (such as equilibrium solutions and their linear stability eigenfunctions), and a method of computing the inner product between velocity fields over the physical domain.

4.1. *Peering into ∞-dimensional state spaces*

Numerical methods have advanced to the point where it is possible to compute highly accurate unstable exact coherent states in low-Reynolds shear flows. How are we to visualize them? Even though fully resolved solutions of the Navier–Stokes equation are embedded in 10^5 or higher dimensional state spaces, there are few unstable eigendirections for Re close to the onset of turbulence. The associated asymptotic strange attractors/repellers might thus be amenable to dynamical systems visualizations, such as trajectory projections, Poincaré sections, state-space partitions and symbolic dynamics descriptions.

In this section, we show that revealing representation-independent state-space portraits can be defined in terms of invariants of the dynamical system. The idea is to form a basis set from fluid states that characterize the recurrent coherent structures, and to project the evolving fluid state $\boldsymbol{u}(t)$ onto this basis with the inner product

$$(\boldsymbol{u}, \boldsymbol{v}) = \frac{1}{V}\int_{\Omega} \mathrm{d}\boldsymbol{x}\ \boldsymbol{u}\cdot\boldsymbol{v}\,, \quad \|\boldsymbol{u}\|^2 = (\boldsymbol{u}, \boldsymbol{u}) \tag{4.1}$$

that corresponds to the energy norm (2.2) and where the fields $\boldsymbol{u}$ and $\boldsymbol{v}$ are differences from the laminar flow. That is, we form orthonormal basis functions $\{\boldsymbol{e}_1, \boldsymbol{e}_2, \ldots, \boldsymbol{e}_n\}$ from a set of linearly independent fluid states and produce a state-space trajectory

$$a(t) = (a_1, a_2, \ldots, a_n, \ldots)(t)\,, \qquad a_n(t) = (\boldsymbol{u}(t), \boldsymbol{e}_n) \tag{4.2}$$

in the $\{\boldsymbol{e}_n\}$ coordinate frame by (4.1). The projection can be viewed in any of the two-dimensional planes $\{\boldsymbol{e}_m, \boldsymbol{e}_n\}$ or in three-dimensional perspective views $\{\boldsymbol{e}_\ell, \boldsymbol{e}_m, \boldsymbol{e}_n\}$. The resulting portraits depend on the fluid states involved and not on the choice of numerical representation. For example, (4.3) defines an orthonormal basis set formed from the upper-branch equilibrium and its four half-cell translations. Orthonormality of the basis set is not strictly necessary, but with it, distances are directly related to the energy norm of $\boldsymbol{u}$.

The low-dimensional projections presented in this section are closely related to other finite approaches to Navier–Stokes in purpose and partly in technique. For example, on a technical level, the projections in this section differ from the finite discretizations discussed in § 3.1 only by degree of dimensionality. If the dimension n of the state-space representation (4.2) were taken to the dimension d of the fully resolved numerical discretization, the two discretizations would be related by a simple linear transformation. To emphasize the differences, we use notation u for the

https://doi.org/10.1017/S002211200800267X Published online by Cambridge University Press

high-dimensional vector of coefficients of a fully resolved numerical discretization, and a for the low-dimensional coordinates of a state-space portrait.

The projection methods here are also similar in spirit to the low-dimensional projections of the Aubry *et al.* (1988) POD modelling approach, in that they aim to capture key features and dynamics of the system in just a few dimensions. Our use of the L^2 inner product, orthonormal basis functions, and the very idea of constructing a basis from characteristic states derive directly from POD modelling. However, the methods presented here depart from the POD in two key points. (i) We construct basis sets from exact solutions of the full-resolved dynamics rather than from the empirical eigenfunctions of the POD. Exact solutions and their linear stability modes (a) characterize coherent fluid states precisely, compared to the truncated expansions of the POD, (b) allow for different basis sets and projections for different purposes and different regions of state space, and (c) are not limited to Fourier modes and $O(2)$ symmetry in homogeneous directions. (ii) We deploy low-dimensional visualization without any low-dimensional modelling. The dynamics are computed with fully resolved direct numerical simulations and projected onto basis sets to produce low-dimensional state-space portraits, tailored to specific purposes and specific regions of state space. The portraits reveal dynamical information visually, providing insight into dynamics that can guide further analysis. We do not suggest that any of our low-dimensional projections is suited to the production of a low-dimensional ODE model via global projection of the state-space dynamics.

4.2. *A global basis spanned by discrete translations of* $\boldsymbol{u}_{UB}$

There is an infinity of possible basis sets, but two choices appear particularly natural: (a) global basis sets, determined by a set of dynamically important and distinct states; or (b) local basis sets, defined in terms of a given equilibrium $\boldsymbol{u}_{EQ}$ and its linear stability eigenfunctions $\boldsymbol{v}_{EQ}^{(n)}$. An example of a local coordinate system based on eigenfunctions of the $\boldsymbol{u}_{UB}$ equilibrium is presented in § 4.4; an example of a global basis is defined here and used to construct state-space portraits in § 4.3.

The projection for a global state-space portrait should emphasize important global features of the flow. For example, for a system with three equilibria, a good first guess for a plane of projection would be the plane containing the three equilibria. The system under study has three distinct equilibria $\boldsymbol{u}_{UB}$, $\boldsymbol{u}_{LB}$and $\boldsymbol{u}_{NB}$, each appearing in four spatial phases, plus the laminar equilibrium at the origin. We have found that for the S-invariant subspace $\mathbb{U}_S$, the irreducible representations of the half-cell translations group T (§ 2.2) provide natural linear combinations of a given equilibrium and its translations.

For example, a set of orthonormal basis functions based on $\boldsymbol{u}_{UB}$ and its half-cell translated siblings can be generated by the four irreducible representations of the D_2 dihedral group $T = \{1, \tau_x, \tau_z, \tau_{xz}\}$ (see § 2.2):

$$\left.\begin{array}{lcccc} & \tau_x & \tau_z & \tau_{xz} & \\ \boldsymbol{e}_1 = c_1(1+\tau_x+\tau_z+\tau_{xz})\,\boldsymbol{u}_{UB} & S & S & S, & \\ \boldsymbol{e}_2 = c_2(1+\tau_x-\tau_z-\tau_{xz})\,\boldsymbol{u}_{UB} & S & A & A, & \\ \boldsymbol{e}_3 = c_3(1-\tau_x+\tau_z-\tau_{xz})\,\boldsymbol{u}_{UB} & A & S & A, & \\ \boldsymbol{e}_4 = c_4(1-\tau_x-\tau_z+\tau_{xz})\,\boldsymbol{u}_{UB} & A & A & S, & \end{array}\right\} \tag{4.3}$$

where c_n is a normalization constant determined by $\|\boldsymbol{e}_n\| = 1$. The last 3 columns indicate the symmetry of each basis function under half-cell translations; e.g. S in the τ_x column implies that $\tau_x \boldsymbol{e}_n = \boldsymbol{e}_n$ and A that $\tau_x \boldsymbol{e}_n = -\boldsymbol{e}_n$. As the 'velocity' $\boldsymbol{u}$ in the Navier–Stokes equation (2.1) for plane Couette flow is the difference from laminar

https://doi.org/10.1017/S002211200800267X Published online by Cambridge University Press

flow, the origin in state-space portraits corresponds to the laminar equilibrium $\boldsymbol{u}_{LM}$. This origin is shared by all symmetry-invariant subspaces, as $\boldsymbol{u}_{LM}=0$ is invariant under all symmetries of the flow. Note, however, that the basis functions $\boldsymbol{e}_n$ are not themselves invariant solutions of Navier–Stokes; rather, they form an orthogonal coordinate system that spans the four translations of $\boldsymbol{u}_{UB}$ within the S-invariant subspace $\mathbb{U}_S$.

The evolution of a state $\boldsymbol{u}\in\mathbb{U}_S$ is represented in this projection by the trajectory $a(t)=(a_1,a_2,a_3,a_4)(t)$ with $a_n(t)=(\boldsymbol{u}(t),\boldsymbol{e}_n)$. As discussed in § 4.1, this is a low-dimensional projection intended for visualization. The dimensionality is lower than the full state space, so trajectories can appear to cross in such projections. We emphasize again that this is one of many possible projections that can be constructed from linear combinations of exact solutions, their spatial translations, and their eigenfunctions. An example of a more complex basis construction is given in § 4.4.

4.3. *A global stroll through plane Couette state space*

With this road map in hand, let us take a stroll through the state space of a transiently turbulent plane Couette flow. Like many dynamical narratives, this will be a long walk through an unfamiliar landscape with many landmarks of local interest. We undertake the tour for several reasons. The main message is that now such a promenade is possible even in 10^5 dimensions. However, a detailed road map is a necessary prerequisite for solving at least three outstanding problems: (*a*) uncovering the interrelations between invariant solutions, such as those of figure 6, (*b*) a partition of state space is a required for a systematic exploration of dynamical invariant structures such as relative periodic orbits, and (*c*) explicit linear stability eigenvectors and their unstable-manifold continuations will be required to control and chaperone a given fluid state to a desired target state.

Our first example of a global state-space portrait of plane Couette flow is figure 5. Here trajectories in the unstable manifolds of $\boldsymbol{u}_{LB}$, $\boldsymbol{u}_{NB}$, $\boldsymbol{u}_{UB}$ and several of their half-cell translations are projected onto the $\{\boldsymbol{e}_1,\boldsymbol{e}_2\}$ plane defined by (4.3). Both $\boldsymbol{e}_1$ and $\boldsymbol{e}_2$ are symmetric in τ_x, so points related by half-cell translations in x (such as $\boldsymbol{u}_{LB}$ and $\tau_x\boldsymbol{u}_{LB}$) map to the same point in this projection. The basis function $\boldsymbol{e}_2$ is antisymmetric in τ_z, so half-cell translations in z appear symmetrically opposite along a_2. $\boldsymbol{u}_{NB}$ and its unstable manifold are shown only in a single z translation, since the reversed orientation of the unstable spiral of $\tau_z\boldsymbol{u}_{NB}$ only clutters the picture.

The $\boldsymbol{u}_{LB}$ unstable manifold W^u_{LB}. This forms the backbone of the dynamics shown in figure 5. The $\boldsymbol{u}_{LB}$ equilibrium has a single real-valued unstable eigenvalue, as shown in figure 4 for $Re=400$ and for much higher Re in Wang *et al.* (2007). W^u_{LB} is therefore one-dimensional and can be computed in its entirety as discussed in § 3.5. In figure 5, the projection of W^u_{LB} onto $\{\boldsymbol{e}_1,\boldsymbol{e}_2\}$ is plotted with thick black lines. Both branches of W^u_{LB} decay to laminar flow, one immediately, and the other after a turbulent excursion towards $\boldsymbol{u}_{UB}$. The portion of the unstable manifold of $\tau_z\boldsymbol{u}_{LB}$ shown here was obtained by applying the τ_z shift, $a_2\to-a_2$, to W^u_{LB}.

We were led to the discovery of $\boldsymbol{u}_{NB}$ by the circular curvature of W^u_{LB} and $\tau_z W^u_{LB}$ in the projection of figure 5, which suggested the possibility of an equilibrium with a complex eigenvalue near the centre of curvature. We initiated Newton-GMRES searches for an equilibrium at several positions between noon and three o'clock along W^u_{LB}, as pictured in figure 5; each search converged either on $\boldsymbol{u}_{LB}$ or on the new equilibrium $\boldsymbol{u}_{NB}$.

The $\boldsymbol{u}_{NB}$ unstable manifold W^u_{NB}. Within $\mathbb{U}_S$, the $\boldsymbol{u}_{NB}$ equilibrium has a complex pair of unstable eigenvalues and one real unstable eigenvalue (figure 4*b*). The instability

https://doi.org/10.1017/S0022112008002677X Published online by Cambridge University Press

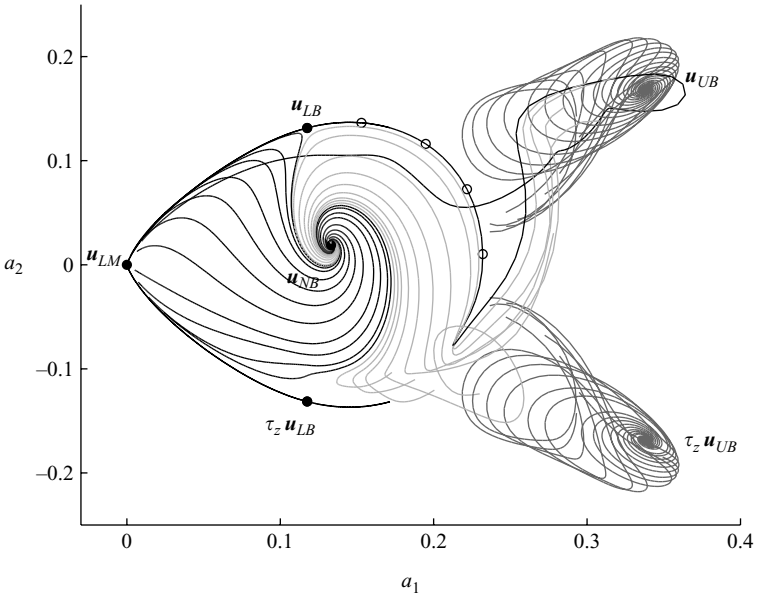


FIGURE 5. A state-space portrait of plane Couette flow for $Re = 400$ and $[L_x, L_y, L_z] = [2\pi/1.14, 2, 4\pi/5]$, projected from 61 506 dimensions to 2. The labelled points are exact equilibrium (steady-state) solutions of the Navier–Stokes equation (see § 3); the curved trajectories are fully resolved time-dependent numerical integrations of Navier–Stokes projected onto the $\boldsymbol{e}_1, \boldsymbol{e}_2$ plane defined by (4.3), with the projection $a_n = (\boldsymbol{u}, \boldsymbol{e}_n)$ defined by (4.1). The laminar equilibrium is $\boldsymbol{u}_{LM}$; the equilibria labelled $\boldsymbol{u}_{LB}$, $\boldsymbol{u}_{NB}$ and $\boldsymbol{u}_{UB}$ are shown in figure 3. W^u_{LB}, the one-dimensional unstable manifold of the 'lower-branch' equilibrium $\boldsymbol{u}_{LB}$, and $\tau_z W^u_{LB}$, its half-cell translation in z, are shown with thick black lines. $W^{u(1,2)}_{NB}$, a two-dimensional portion of the unstable manifold of $\boldsymbol{u}_{NB}$, is shown with thin black and grey spirals emanating from $\boldsymbol{u}_{NB}$. Similarly, the dark grey lines spiralling out of $\boldsymbol{u}_{UB}$ and $\tau_z \boldsymbol{u}_{UB}$ indicate $W^{u,S}_{UB}$ and $\tau_z W^{u,S}_{UB}$, the two-dimensional unstable manifolds of $\boldsymbol{u}_{UB}$ and its half-cell translation $\tau_z \boldsymbol{u}_{UB}$. Open dots along W^u_{LB} show initial conditions for Newton-GMRES searches used to find $\boldsymbol{u}_{NB}$. The plane of the projection is defined in terms of the equilibrium solutions; it is dynamically invariant and independent of the numerical representation. See §§ 4.2, 4.3 and 3.2 for discussions of the projection, dynamics and numerical discretization.

of the real eigenvalue is weaker than the complex pair; we omit it from consideration here and focus on the two-dimensional subset $W^{u(1,2)}_{NB}$ corresponding to the complex pair $\lambda^{(1,2)}_{NB}$ with eigenvectors $v^{(1,2)}_{NB}$. $W^{u(1,2)}_{NB}$ is shown in figure 5 as a spiral of trajectories emanating from $\boldsymbol{u}_{NB}$, calculated as discussed in § 3.5. This simple geometric picture produces our first striking result: the two-dimensional surface $W^{u(1,2)}_{NB}$ is apparently bounded by the one-dimensional curve W^u_{LB}.

A heteroclinic connection from $\boldsymbol{u}_{NB}$ *to* $\boldsymbol{u}_{LB}$. As it approaches $\boldsymbol{u}_{LB}$, $W^{u(1,2)}_{NB}$ separates along the two branches of W^u_{LB}. Since $\boldsymbol{u}_{LB}$ has a single unstable eigenvalue, we expect that a single trajectory in $W^{u(1,2)}_{NB}$ straddles the split along W^u_{LB} and is drawn in towards $\boldsymbol{u}_{LB}$ along its stable eigenvectors as $t \to \infty$, forming a heteroclinic connection from $\boldsymbol{u}_{NB}$ to $\boldsymbol{u}_{LB}$.

This is an unexpected result. In dimensions higher than two, heteroclinic connections are non-generic, since it is unusual that a one-dimensional trajectory can be arranged to strike a particular zero-dimensional point. However, discrete symmetries and the dimensionality of the $\boldsymbol{u}_{LB}$ unstable manifold make heteroclinic connections possible in this case (Kevrekidis, Nicolaenko & Scovel 1990; Holmes *et al.* 1996; Cvitanović

https://doi.org/10.1017/S002211200800267X Published online by Cambridge University Press

et al. 2008). The set of candidate trajectories emerging from the neighbourhood of $\boldsymbol{u}_{NB}$ is increased from one dimension to two by the complex instability (or three if $\lambda^{(3)}_{NB}$ is considered as well). The dimensionality of state space near the target $\boldsymbol{u}_{LB}$ is effectively reduced to one by its codimension-1 set of stable eigenvalues.

Considered in the full space $\mathbb{U}$, the continuous translation symmetry increases the dimensionality of both the candidate trajectories and the target by two. However, the invariance of $\mathbb{U}_S$ under Navier–Stokes immediately restricts possible heteroclinic connections between $\boldsymbol{u}_{NB}$ and the torus of $\boldsymbol{u}_{LB}$ translations to the four translations of $\boldsymbol{u}_{LB}$ within $\mathbb{U}_S$: if a trajectory in the unstable manifold of $\boldsymbol{u}_{NB}$ terminates at a $\boldsymbol{u}_{LB}$ state, it may do so only at $\boldsymbol{u}_{LB}$, $\tau_x\boldsymbol{u}_{LB}$, $\tau_z\boldsymbol{u}_{LB}$, or $\tau_{xz}\boldsymbol{u}_{LB}$. Note also that most weakly stable eigenvalues of $\boldsymbol{u}_{LB}$, $\lambda^{(4)}_{LB}$ through $\lambda^{(8)}_{LB}$, are outside the $\mathbb{U}_S$ subspace, so trajectories in $W^{u(1,2)}_{NB}$ are forced to approach $\boldsymbol{u}_{LB}$ along the more strongly contracting eigendirections of $\lambda^{(9)}_{LB}$ and $\lambda^{(10)}_{LB}$ (table 1).

The heteroclinic connection from $\boldsymbol{u}_{NB}$ to $\boldsymbol{u}_{LB}$ forms a boundary between trajectories that decay immediately to laminar flow and those that grow towards transient turbulence. Those that pass near $\boldsymbol{u}_{LB}$ and grow to turbulence follow the unstable manifold of $\boldsymbol{u}_{LB}$ into a region near the $\boldsymbol{u}_{UB}$ equilibrium. For $Re = 400$ and $[L_x, L_y, L_z] = [2\pi/1.14, 2, 4\pi/5]$, all generic initial conditions investigated so far ultimately decay to laminar. However, at higher Reynolds numbers and larger aspect ratios for which turbulence is sustained, we expect that the $\boldsymbol{u}_{NB} \to \boldsymbol{u}_{LB}$ heteroclinic connection will form a one-dimensional portion of the boundary of the laminar state's basin of attraction. This one-dimensional boundary should be extendable to two dimensions by taking the third unstable eigenvalue of $\boldsymbol{u}_{NB}$ into consideration.

Lastly, we note that it is not possible to determine from figure 5 alone whether the heteroclinic connection from $\boldsymbol{u}_{NB}$ goes to $\boldsymbol{u}_{LB}$ or $\tau_x\boldsymbol{u}_{LB}$, since both of these map to the same point in the $\{\boldsymbol{e}_1, \boldsymbol{e}_2\}$ plane of projection. Figure 6 (discussed below) resolves this question and shows that the connection is indeed from $\boldsymbol{u}_{NB}$ to $\boldsymbol{u}_{LB}$.

Dynamics near $\tau_z\boldsymbol{u}_{LB}$ and $\tau_{xz}\boldsymbol{u}_{LB}$. A second separation of $\boldsymbol{u}_{NB}$'s unstable manifold $W^{u(1,2)}_{NB}$ occurs in the bottom half of figure 5, near $\tau_z\boldsymbol{u}_{LB}$. Trajectories on the laminar side of $\tau_z\boldsymbol{u}_{LB}$ follow its unstable manifold towards the laminar state; those on the other side head towards turbulence in the direction of the $\tau_z\boldsymbol{u}_{LB}$ unstable manifold.

The dynamics in the region near $\tau_z\boldsymbol{u}_{LB}$ can be clarified by adding a third coordinate $a_3 = (\boldsymbol{u}, \boldsymbol{e}_3)$ to the two-dimensional projection of figure 5. Since $\boldsymbol{e}_3$ is antisymmetric in τ_x, the a_3 coordinate distinguishes states such as $\tau_z\boldsymbol{u}_{LB}$ and $\tau_{xz}\boldsymbol{u}_{LB}$ that are related by a τ_x translation and so lie on top of each other in the projection of figure 5: $(\tau_z\boldsymbol{u}_{LB}, \boldsymbol{e}_3) = -(\tau_{xz}\boldsymbol{u}_{LB}, \boldsymbol{e}_3)$. Figure 6 shows a three-dimensional perspective of (a_1, a_2, a_3) which reveals that the second separation of $W^{u(1,2)}_{NB}$, unlike the first, does not result from a heteroclinic connection between $\boldsymbol{u}_{NB}$ and a translation of $\boldsymbol{u}_{LB}$. As trajectories straddling the split near $\tau_z\boldsymbol{u}_{LB}$ and $\tau_{xz}\boldsymbol{u}_{LB}$ are refined, they approach neither of these points. Likewise, the extensions of the refined trajectories approach neither the $W^u_{\tau_z LB} = \tau_z W^u_{LB}$ nor $W^u_{\tau_{xz}LB} = \tau_{xz}W^u_{LB}$ unstable manifolds. The thick grey trajectory in figure 6 passes closer to $\tau_{xz}\boldsymbol{u}_{LB}$ than the other trajectories shown, but it recedes from $\tau_{xz}W^u_{LB}$ instead of approaching it.

The geometry of $W^{u(1,2)}_{NB}$ in this region is fairly complex. The separation of trajectories between $\tau_z\boldsymbol{u}_{LB}$ and $\tau_{xz}\boldsymbol{u}_{LB}$ suggests that another equilibrium might exist in this region; however, all Newton-GMRES searches initiated in this region converged on $\tau_z\boldsymbol{u}_{LB}$ or $\tau_{xz}\boldsymbol{u}_{LB}$. It is clear, however, that the geometry of $W^{u(1,2)}_{NB}$ is shaped by the unstable manifolds of $\boldsymbol{u}_{LB}$ and two of its translations, namely, W^u_{LB}, $W^u_{\tau_z LB}$, and $W^u_{\tau_{xz}LB}$. The upper-branch solution also plays a role: in figure 5, one trajectory within $W^{u(1,2)}_{NB}$ is drawn towards $\tau_z\boldsymbol{u}_{UB}$ and follows trajectories in its unstable manifold. The

https://doi.org/10.1017/S002211200800267X Published online by Cambridge University Press

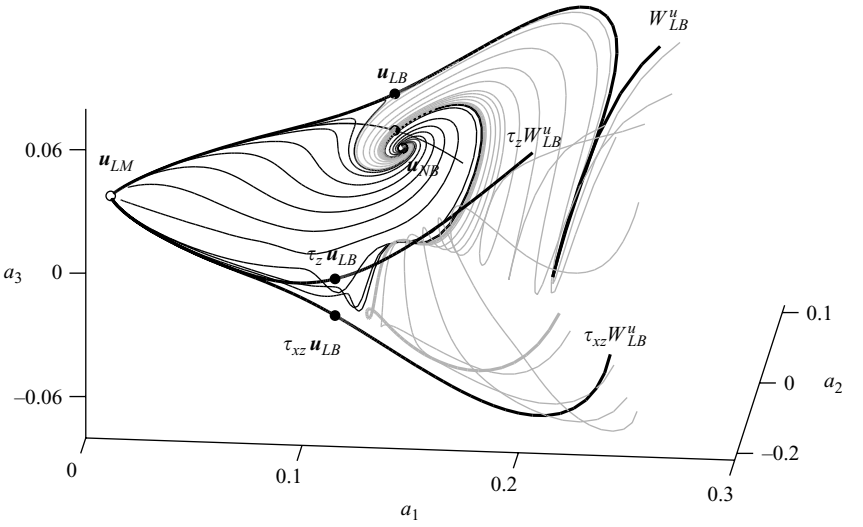


FIGURE 6. The unstable manifold of $\boldsymbol{u}_{LB}$ and its half-cell translations W^u_{LB}, $\tau_{xz} W^u_{LB}$, etc. (thick black lines) and a two-dimensional portion of the $\boldsymbol{u}_{NB}$ unstable manifold $W^{u(1,2)}_{NB}$ (thin black and grey lines). $\boldsymbol{u}_{NB}$ is shown in only one translation (centre of spiral); all four translations of $\boldsymbol{u}_{LB}$ are shown (solid dots – the unlabelled dot underneath $\boldsymbol{u}_{LB}$ is $\tau_x \boldsymbol{u}_{LB}$). The thick grey line makes the closest pass to $\tau_{xz} \boldsymbol{u}_{LB}$ of the trajectories shown. The projection is from 61 506 dimensions to 3 in the translation-symmetric global basis $\{\boldsymbol{e}_1, \boldsymbol{e}_2, \boldsymbol{e}_3\}$ defined by (4.3).

perspective of figure 6 also identifies $\boldsymbol{u}_{LB}$ and not $\tau_x \boldsymbol{u}_{LB}$ as the endpoint of the heteroclinic connection discussed above.

Thus, with two simple state-space portraits, we have identified several regions in state space that trigger transitions toward qualitatively different types of flow. We expect that identification of such state-space regions will be extremely valuable in the development of nonlinear control strategies for wall-bounded turbulence.

4.4. *A local state-space portrait: the unstable manifold of* $\boldsymbol{u}_{UB}$ *in* $\mathbb{U}_S$

The eigenfunctions of an equilibrium provide a natural coordinate system for viewing its local dynamics. Within the S-invariant subspace $\mathbb{U}_S$, $\boldsymbol{u}_{UB}$ has a single complex pair of unstable eigenvalues, which define a plane of local linear oscillation and two natural directions for a local coordinate system. The two-dimensional portion of W^u_{UB} within $\mathbb{U}_S$, which we denote by $W^{u,S}_{UB}$, departs from this plane as the distance from $\boldsymbol{u}_{UB}$ increases and the magnitudes of nonlinear terms in the local Taylor expansion become non-negligible. However, since the nature of this nonlinearity was unknown, it was not immediately clear in our investigations how to choose a third basis function for a three-dimensional projection of local $\boldsymbol{u}_{UB}$ dynamics. We tried a variety of candidates, including principal components analysis (i.e. local POD) on numerically integrated trajectories as they deviate from the plane of oscillation. This initial exploration suggested that the dominant nonlinear effects about $\boldsymbol{u}_{UB}$ are in fact the linearized dynamics around its half-cell translation $\tau_x \boldsymbol{u}_{UB}$.

We then constructed a basis set by Gram–Schmidt orthogonalization of the plane of oscillation $\boldsymbol{v}^{(1)}_{r,UB}$, $\boldsymbol{v}^{(1)}_{i,UB}$ of the unstable complex eigenvalue pair $\lambda^{(1,2)}_{UB}$ (see § 3.5) and $(\tau_x \boldsymbol{u}_{UB} - \boldsymbol{u}_{UB})$, that is, the direction between $\boldsymbol{u}_{UB}$ and its half-cell translation in x. We indicate the Gram–Schmidt orthogonalized basis and coordinates with a

https://doi.org/10.1017/S002211200800267X Published online by Cambridge University Press

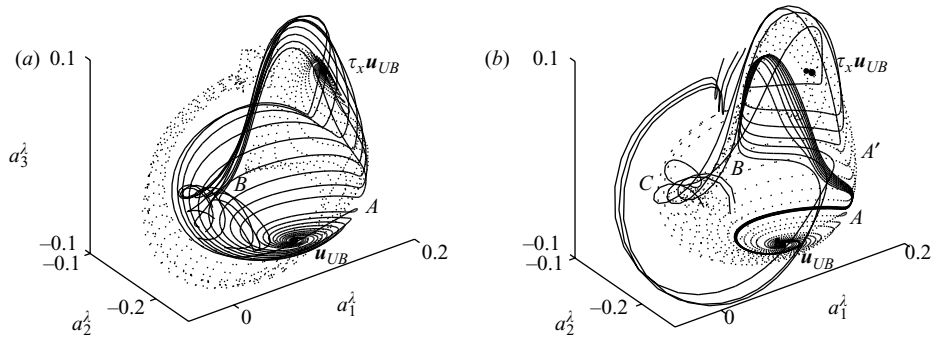


FIGURE 7. (*a*) The unstable manifolds $W^{u,S}_{UB}$ (solid lines) and $\tau_x W^{u,S}_{UB}$ (dotted lines) of the upper-branch equilibrium $\boldsymbol{u}_{UB}$ and its half-cell translation $\tau_x \boldsymbol{u}_{UB}$. (*b*) A refined view of dynamics within $W^{u,S}_{UB}$. The coordinates $(a_1^\lambda, a_2^\lambda, a_3^\lambda)$ are projections onto the basis set $\{\boldsymbol{e}_1^\lambda, \boldsymbol{e}_2^\lambda, \boldsymbol{e}_3^\lambda\}$ that spans the plane of unstable oscillation around $\boldsymbol{u}_{UB}$ and the direction between $\boldsymbol{u}_{UB}$ and $\tau_x \boldsymbol{u}_{UB}$. See § 4.4.

λ superscript, $\{\boldsymbol{e}_1^\lambda, \boldsymbol{e}_2^\lambda, \boldsymbol{e}_3^\lambda\}$ and $a_n^\lambda(t) = (\boldsymbol{u}(t), \boldsymbol{e}_n^\lambda)$, to indicate its construction from the unstable $\boldsymbol{u}_{UB}$ eigenfunctions and the $\boldsymbol{u}_{UB}$ to $\tau_x \boldsymbol{u}_{UB}$ line.

Figure 7 shows $W^{u,S}_{UB}$ in the $\boldsymbol{e}_n^\lambda$ local coordinate system. In figure 7(*a*), $W^{u,S}_{UB}$ spirals out from the centre $\boldsymbol{u}_{UB}$ in the plane $\{\boldsymbol{e}_1^\lambda, \boldsymbol{e}_2^\lambda\}$ spanning $\boldsymbol{v}^{(1)}_{r,UB}, \boldsymbol{v}^{(1)}_{i,UB}$. Strong nonlinearity and strong trajectory separation first occur near point A: below A, trajectories continue the unstable linear oscillation for another cycle; above, they begin oscillation around $\tau_x \boldsymbol{u}_{UB}$, following paths similar to trajectories in $\tau_x W^u_{\boldsymbol{u}_{UB}}$. Figure 7(*b*) shows a refinement of trajectories in $W^{u,S}_{UB}$ on the upper side of the split at A. Near point B, the refined trajectories undergo a second split from their neighbours (figure 7*a*), and a third split among themselves at A'. This behaviour and marked similarity to the trajectories of $\tau_x W^{u,S}_{UB}$ in figure 7(*a*) suggests that dynamics in this region, until escape, consists of alternating oscillations around a symmetric pair of unstable equilibrium, in a manner reminiscent of the Lorenz system.

This interpretation is reinforced by figure 8, which shows the pair of $W^{u,S}_{UB}$ trajectories from figure 7(*b*) that split at A' together with their counterparts in $\tau_x W^{u,S}_{UB}$, replotted using the global translational–symmetric basis (4.3). The projection onto $(\boldsymbol{e}_1 + \boldsymbol{e}_2)/\sqrt{2}$ and $\boldsymbol{e}_3$ was chosen because it provides a clear view of the path ABA', and because these basis functions are symmetric and antisymmetric in τ_x, respectively. Note that the two pairs of trajectories in $W^{u,S}_{UB}$ and $\tau_x W^{u,S}_{UB}$ draw together just before A'. Each pair of nearby trajectories emanating from the same equilibrium splits at A' and switches allegiance with the pair from the opposite equilibrium, so that past A', trajectories on opposite unstable manifolds follow almost identical paths. The τ_x-antisymmetric long-term behaviour of two nearby initial conditions from $\boldsymbol{u}_{UB}$ suggests that the path from B to A' is one of weakening x variation, reaching small but nearly τ_x-antisymmetric x variation near A'. After A', a τ_x-antisymmetric instability comes into play, resulting in long-term τ_x-antisymmetric dynamics.

For the parameters of this study, the trajectories investigated so far leave the region of the $\boldsymbol{u}_{UB}$ and its translations after a few oscillations, so that the $\boldsymbol{u}_{UB}$ unstable manifold has the characteristics of a chaotic repeller. We expect that unstable periodic orbits can be found in this region, and we intend to explore this in a future paper.

https://doi.org/10.1017/S002211200800267X Published online by Cambridge University Press

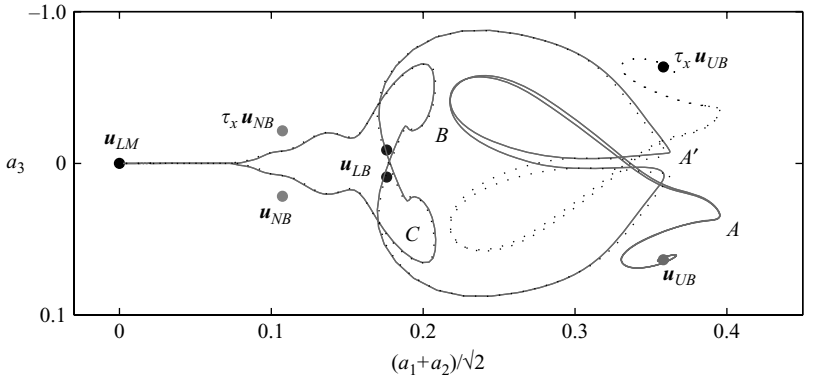


FIGURE 8. A pair of nearby trajectories in the unstable manifold of $\boldsymbol{u}_{UB}$, from figure 7(*a*) (solid, black), plotted against their symmetric counterparts in the unstable manifold of $\tau_x \boldsymbol{u}_{UB}$ (dotted, black), together with $\boldsymbol{u}_{LB}$ and $\tau_x \boldsymbol{u}_{LB}$ (black dots, latter unlabelled), $\boldsymbol{u}_{NB}$ and $\tau_x \boldsymbol{u}_{UB}$ (grey dots), and the laminar equilibrium $\boldsymbol{u}_{LM}$ (black dot). $\boldsymbol{u}_{NB}$ appears much closer to the laminar state than $\boldsymbol{u}_{LB}$ by an artefact of the projection; see figure 5 for another view. The coordinates a_1, a_2 are in the global translation-symmetric basis $\boldsymbol{e}_1, \boldsymbol{e}_2$ defined by (4.3) and used in figures 5 and 6.

4.5. *Transient turbulence*

The final stop in our stroll through plane Couette state space is an illustration of transient turbulence against the backdrop of the invariant structures featured in previous figures. Figure 9(*a*) shows a single trajectory, initiated as a perturbation of $\boldsymbol{u}_{NB}$, that exhibits transient turbulence and then decays to laminar flow. The coordinate system is (4.3), the same as in figure 6. The region of state space explored by this trajectory is typical of all observed transiently turbulent dynamics in $\mathbb{U}_S$. The trajectory is unusually long-lived; after leaving the spiralling region around $\boldsymbol{u}_{NB}$ it wanders for some 1000 non-dimensionalized L/U time units before converging on the laminar state, compared to a more typical 200 time-unit lifetimes of other trajectories initialized as perturbations of $\boldsymbol{u}_{NB}$.

When seen in isolation in figure 9(*a*), the turbulent trajectory shows little discernible order. When plotted within the framework of invariant structures of the flow, in figure 9(*b*), structure is immediately evident. In this three-dimensional perspective, the decay to laminar flow is confined to a region bounded by the $\boldsymbol{u}_{NB}$ and $\boldsymbol{u}_{LB}$ unstable manifolds. Transient turbulence occurs on the far side of laminar from these states, $a_1 > 0.15$, and in a region shaped roughly by the unstable manifolds of $\boldsymbol{u}_{LB}$, $\boldsymbol{u}_{UB}$, $\boldsymbol{u}_{NB}$, and their half-box translations. Close inspection shows that segments of the transient turbulent trajectory occasionally follow the contours of nearby unstable manifolds.

5. Conclusion and perspectives

Currently, a large conceptual gap separates what has been achieved for low-dimensional dynamical systems and the challenges we face in understanding infinite-dimensional turbulent flows. Recent computations of invariant solutions of wall-bounded flows and their agreement with the qualitative features of numerical simulations and experiments suggest that a dynamical theory of moderate-*Re* turbulence is within reach. We initiate a systematic exploration of the hierarchy of

https://doi.org/10.1017/S002211200800267X Published online by Cambridge University Press

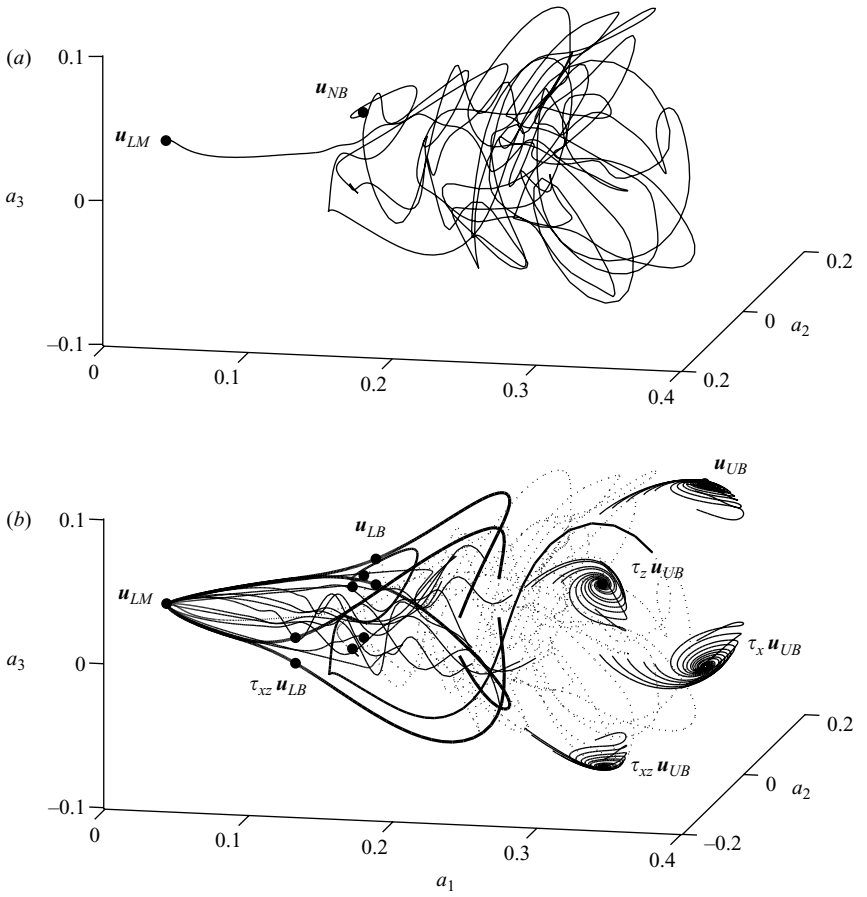


FIGURE 9. A transiently turbulent trajectory in the $\boldsymbol{u}_{NB}$ unstable manifold, (*a*) in isolation (*b*) in relation to $\boldsymbol{u}_{LB}$, $\boldsymbol{u}_{NB}$, $\boldsymbol{u}_{UB}$, their half-cell translations, and their unstable manifolds (see figures 5 and 6 for more detailed labelling of these features). The final decay to laminar of several other trajectories in the unstable manifolds of $\boldsymbol{u}_{NB}$ and $\boldsymbol{u}_{UB}$ are also shown. The projection is the same as that of figure 6.

exact unstable invariant solutions of fully resolved Navier–Stokes equations in order to describe the spatio-temporally chaotic dynamics of turbulent fluid flows in terms of these states. The key advance reported here is a novel visualization of moderate-*Re* fluid dynamics in terms of dynamically invariant, intrinsic and representation independent coordinate frames. The method offers an alternative visualization of numerical and/or experimental data of any dissipative flow close to the onset of turbulence. In this paper, the visualizations led to the discovery of a new equilibrium solution of plane Couette flow and a heteroclinic connection between two non-laminar equilibria. We have also computed the eigenvalues and symmetries of the three known equilibria of plane Couette flow in a small periodic cell with moderate Reynolds number and established the low-dimensionality of their unstable manifolds.

At first glance, turbulent dynamics visualized in state space might appear hopelessly complex, but detailed examination suggests it might be much less so than feared: turbulent dynamics appears to be pieced together from near visitations to exact coherent states interspersed by transient interludes. Equilibria, travelling waves, and

https://doi.org/10.1017/S002211200800267X Published online by Cambridge University Press

periodic solutions of plane Couette flow embody Hopf's vision: a repertoire of recurrent spatio-temporal patterns explored by turbulent dynamics. We conceive of turbulence as a walk through a repertoire of unstable recurrent patterns. As a turbulent flow evolves, every so often we catch a glimpse of a familiar pattern. For any finite spatial resolution, the flow approximately follows for a finite time a pattern belonging to a finite alphabet of admissible fluid states, represented here by a set of exact coherent states.

What new insights does the 'unstable coherent states program' offer? Normal-form models derived from severe truncations of spectral representations of PDEs – most famously the Lorenz model – capture qualitatively the bifurcations and chaotic dynamics evocative of those observed in fluid dynamics. In contrast, exact unstable coherent states and periodic orbit theory should provide accurate quantitative predictions for dynamical observables of Navier–Stokes (such as the average turbulent drag), for a given flow, flow geometry, Re and other parameters. This description should lead to quantitative predictions of transport properties of fluid flows such as bulk flow rate, mean wall drag, and their fluctuations. The success of computing exact eigenfunctions and unstable manifolds also opens a new approach to control of turbulence in wall-bounded shear flows: perturbations in these directions can be used to stabilize or chaperone the flow towards a desired fluid state, and not necessarily the laminar one (Kawahara, Kida & Nagata 2005; Wang *et al.* 2007).

The state-space exploration of equilibria and their global unstable manifolds presented here is the first step. Although important in organizing the turbulent flow, equilibria, being static, do not actually participate in it. That role is played by the infinity of unstable periodic orbits densely embedded in the asymptotic attractor. That it is possible to compute exact three-dimensional unstable periodic solutions of Navier–Stokes has been demonstrated in the pioneering work of Kawahara & Kida (2001), for periodic orbits, and Viswanath (2007), for relative periodic orbits. However, a combination of novel and proven numerical and analytical techniques such as variational solvers, periodic orbit theory and group representation theory is still required for a systematic exploration of the hierarchy of such solutions and to derive the statistics of the flow through periodic orbit theory (Cvitanović *et al.* 2007).

We would like to acknowledge F. Waleffe for his very generous guidance through the course of this research. We also greatly appreciate D. Viswanath's guidance in the linearized stability calculations and his thoughtful comments on drafts. We are very grateful for the valuable comments and suggestions of the reviewers. P. C. and J. F. G. thank G. Robinson, Jr for support. J. H. thanks R. Mainieri and T. Brown, Institute for Physical Sciences, for partial support.

Appendix. Tabulation of numerical results

Tables 1 and 2 give the least stable linear stability eigenvalues of the $\boldsymbol{u}_{LM}$, $\boldsymbol{u}_{LB}$, $\boldsymbol{u}_{NB}$ and $\boldsymbol{u}_{UB}$ equilibria, together with symmetries of corresponding eigenfunctions. The unstable eigenvalues together with a set of the least contracting stable eigenvalues are also shown in figure 4. All numerical results tabulated in this Appendix are computed for plane Couette flow with $Re = 400$ and $[L_x, L_y, L_z] = [2\pi/1.14, 2, 4\pi/5]$. Full sets of exact invariant solutions, their linear stability eigenvalues and eigenfunctions are available on `channelflow.org`, (Gibson 2007), or can be obtained by a request to the authors.

https://doi.org/10.1017/S002211200800267X Published online by Cambridge University Press

(*a*)

n	Mode	k_y	k_z	Arnoldi $\lambda_{LM}^{(n)}$	Analytic $\lambda_{LM}^{(n)}$
1, 2	H	1	0	−0.00616850	−0.00616850
3, 4	H	1	1	−0.02179322	−0.02179350
5, 6	H	2	0	−0.02467398	−0.02467401
7, 8	S	–	1	−0.02916371	−0.02916371
9, 10	H	2	1	−0.04029896	−0.04029901
11, 12	H	3	0	−0.05551652	−0.05551653

(*b*)

n	$\mu_{LB}^{(n)}$	$\omega_{LB}^{(n)}$	s_1	s_2	s_3
1	0.0501205		S	S	S
2	10^{-6}			–	
3	10^{-6}			–	
4	−0.0020054		A	S	A
5	−0.0065977		A	A	S
6	−0.0069308		S	A	A
7	−0.0097953		S	A	A
8	−0.0135925		A	S	A
9	−0.0239353		S	S	S
10	−0.0335130		S	S	S
11	−0.0370295		S	A	A
12, 13	−0.0454857	0.0190660	A	A	S

TABLE 1. (*a*) Least stable eigenvalues of the laminar equilibrium $\boldsymbol{u}_{LM}$ for $[L_x, L_y, L_z] = [2\pi/1.14, 2, 4\pi/5]$ and $Re = 400$, computed by Arnoldi iteration, compared to Stokes (S) and heat-equation (H) eigenvalues from analytic formulae. This serves as a test of accuracy for our numerical algorithms. The heat-equation eigenfunctions have the form $\boldsymbol{u}(\boldsymbol{x}, t) = \mathrm{e}^{\lambda t} \sin(\pi k_y y/2) \cos(2\pi k_z z/L_z)\, \hat{\boldsymbol{x}}$ for k_y even and $\mathrm{e}^{\lambda t} \cos(\pi k_y y/2) \cos(2\pi k_z z/L_z))\, \hat{\boldsymbol{x}}$ for k_y odd, and eigenvalues $\lambda = -(\pi^2 {k_y}^2/4 + 4\pi^2 {k_z}^2/{L_z}^2)/Re$. The Stokes eigenvalue listed is the lowest-order mode with v component of the form $\hat{v}(y) \cos(2\pi z/L_z)$, $\hat{v}(y)$ even in y (see Waleffe 1997). The eigenvalues are ordered in the table by decreasing real part. All laminar eigenvalues are real. (*b*) $\boldsymbol{u}_{LB}$ equilibrium stability eigenvalues $\lambda = \mu \pm \mathrm{i}\omega$ and symmetries of corresponding eigenvectors at same parameter values. The zero eigenvalues result from the continuous translation symmetry of the flow.

(*a*)

n	$\mu_{NB}^{(n)}$	$\omega_{NB}^{(n)}$	s_1	s_2	s_3
1	0.0306497		A	S	A
2, 3	0.0261952	0.056377	S	S	S
4	0.0183668		S	S	S
5	0.0174064		S	A	A
6	0.0158648		A	A	S
7	10^{-7}			–	
8	10^{-7}			–	
9	−0.0045203		A	S	A
10	−0.0048642		S	A	A

(*b*)

n	$\mu_{UB}^{(n)}$	$\omega_{UB}^{(n)}$	s_1	s_2	s_3
1	0.0555837		A	A	S
2, 3	0.0325292	0.107043	S	S	S
4, 5	0.0160591	0.039238	S	A	A
6, 7	0.0152926	0.284177	S	A	A
8	0.0106036		A	S	A
9	10^{-6}			–	
10	10^{-7}			–	
11, 12	−0.0141215	0.057748	S	S	S
13	−0.0181827		S	A	A

TABLE 2. Stability eigenvalues $\lambda = \mu \pm \mathrm{i}\omega$ and symmetries of corresponding eigenvectors: (*a*) $\boldsymbol{u}_{NB}$, (*b*) $\boldsymbol{u}_{UB}$ equilibrium for $[L_x, L_y, L_z] = [2\pi/1.14, 2, 4\pi/5]$ and $Re = 400$.

REFERENCES

AUBRY, N., HOLMES, P., LUMLEY, J. L. & STONE, E. 1988 The dynamics of coherent structures in the wall region of turbulent boundary layer. *J. Fluid Mech.* **192**, 115–173.

BARENGHI, C. 2004 Turbulent transition for fluids. *Phys. World* **17** (12), 17–18.

BUSSE, F. H. 2004 Visualizing the dynamics of the onset of turbulence. *Science* **305**, 1574–1575.

CHRISTIANSEN, F., CVITANOVIĆ, P. & PUTKARADZE, V. 1997 Spatio-temporal chaos in terms of unstable recurrent patterns. *Nonlinearity* **10**, 55–70.

CLEVER, R. M. & BUSSE, F. H. 1992 Three-dimensional convection in a horizontal layer subjected to constant shear. *J. Fluid Mech.* **234**, 511–527.

https://doi.org/10.1017/S002211200800267X Published online by Cambridge University Press

Cvitanović, P., Artuso, R., Mainieri, R., Tanner, G., Vattay, G., Whelan, N. & Wirzba, A. 2007 *Chaos: Classical and Quantum*. Niels Bohr Institute, Copenhagen. ChaosBook.org.

Cvitanović, P., Davidchack, R. L. & Siminos, E. 2008 State space geometry of a spatio-temporally chaotic Kuramoto-Sivashinsky flow. Available at arxiv.org:0709.2944.

Dauchot, O. & Vioujard, N. 2000 Phase space analysis of a dynamical model for the subcritical transition to turbulence in plane Couette flow. *Eur. Phys. J.* B **14**, 377–381.

Faisst, H. & Eckhardt, B. 2003 Traveling waves in pipe flow. *Phys. Rev. Lett.* **91**, 224502.

Foias, C., Nicolaenko, B., Sell, G. R. & Temam, R. 1985 Inertial manifold for the Kuramoto–Sivashinsky equation. *C. R. Acad. Sci. I-Math* **301**, 285–288.

Gibson, J. F. 2002 Dynamical systems models of wall-bounded, shear-flow turbulence. PhD thesis, Cornell University.

Gibson, J. F. 2007 Channelflow: a spectral Navier–Stokes simulator in C++. *Tech. Rep.* Georgia Institute of Technology.

Golubitsky, M. & Stewart, I. 2002 *The Symmetry Perspective*. Birkhäuser, Boston.

Halcrow, J. 2008 Geometry of turbulence: an exploration of the state-space of plane Couette flow. PhD thesis, School of Physics, Georgia Institute of Technology, Atlanta. ChaosBook.org/projects/theses.html.

Hamilton, J. M., Kim, J. & Waleffe, F. 1995 Regeneration mechanisms of near-wall turbulence structures. *J. Fluid Mech.* **287**, 317–348.

Hof, B., van Doorne, C. W. H., Westerweel, J., Nieuwstadt, F. T. M., Faisst, H., Eckhardt, B., Wedin, H., Kerswell, R. R. & Waleffe, F. 2004 Experimental observation of nonlinear traveling waves in turbulent pipe flow. *Science* **305** (5690), 1594–1598.

Holmes, P., Lumley, J. L. & Berkooz, G. 1996 *Turbulence, Coherent Structures, Dynamical Systems and Symmetry*. Cambridge University Press.

Hopf, E. 1948 A mathematical example displaying features of turbulence. *Commun. Appl. Maths* **1**, 303–322.

Itano, T. & Toh, S. 2001 The dynamics of bursting process in wall turbulence. *J. Phys. Soc. Japan* **70**, 703–716.

Jiménez, J., Kawahara, G., Simens, M. P., Nagata, M. & Shiba, M. 2005 Characterization of near-wall turbulence in terms of equilibrium and bursting solutions. *Phys. Fluids* **17**, 015105.

Kawahara, G. & Kida, S. 2001 Periodic motion embedded in plane Couette turbulence: regeneration cycle and burst. *J. Fluid Mech.* **449**, 291–300.

Kawahara, G., Kida, S. & Nagata, M. 2005 Unstable periodic motion in plane Couette system: the skeleton of turbulence. In *One Hundred Years of Boundary Layer Research*. Kluwer.

Kerswell, R. R. & Tutty, O. 2007 Recurrence of travelling wave solutions in transitional pipe flow. *J. Fluid Mech.* **584**, 69–102.

Kevrekidis, I. G., Nicolaenko, B. & Scovel, J. C. 1990 Back in the saddle again: a computer assisted study of the Kuramoto–Sivashinsky equation. *SIAM J. Appl. Maths.* **50**, 760–790.

Kim, J., Moin, P. & Moser, R. 1987 Turbulence statistics in fully developed channel flow at low Reynolds number. *J. Fluid Mech.* **177**, 133–166.

Kleiser, L. & Schumann, U. 1980 Treatment of incompressibility and boundary conditions in 3-D numerical spectral simulations of plane channel flows. In *Proc. 3rd GAMM Conf. Numerical Methods in Fluid Mechanics* (ed. E. Hirschel), pp. 165–173. GAMM, Viewweg, Braunschweig.

Kline, S. J., Reynolds, W. C., Schraub, F. A. & Rundstadler, P. W. 1967 The structure of turbulent boundary layers. *J. Fluid Mech.* **30**, 741–773.

Li, W. & Graham, M. 2007 Polymer induced drag reduction in exact coherent structures of plane Poiseuille flow. *Phys. Fluids* **19** (083101), 1–15.

López, V., Boyland, P., Heath, M. T. & Moser, R. D. 2006 Relative periodic solutions of the complex Ginzburg–Landau equation. *SIAM J. Appl. Dyn. Systems* **4**, 1042–1075.

Manneville, P. 2004 Spots and turbulent domains in a model of transitional plane Couette flow. *Theoret. Comput. Fluid Dyn.* **18**, 169–181.

Moehlis, J., Faisst, H. & Eckhardt, B. 2004 A low-dimensional model for turbulent shear flows. *New J. Phys.* **6**, 56.

Moehlis, J., Faisst, H. & Eckhardt, B. 2005 Periodic orbits and chaotic sets in a low-dimensional model for shear flows. *SIAM J. Appl. Dyn. Systems* **4**, 352–376.

Nagata, M. 1990 Three-dimensional finite-amplitude solutions in plane Couette flow: bifurcation from infinity. *J. Fluid Mech.* **217**, 519–527.

https://doi.org/10.1017/S002211200800267X Published online by Cambridge University Press

Nagata, M. 1997 Three-dimensional traveling-wave solutions in plane Couette flow. *Phys. Rev.* E **55**, 2023–2025.

Panton, R. L. (ed.) 1997 *Self-Sustaining Mechanisms of Wall Turbulence*. Computational Mechanics, Southhampton.

Robinson, S. K. 1991 Coherent motions in the turbulent boundary layer. *Annu. Rev. Fluid Mech.* **23**, 601–639.

Schmiegel, A. 1999 Transition to turbulence in linearly stable shear flows. PhD thesis, Philipps-Universität Marburg.

Schmiegel, A. & Eckhardt, B. 1997 Fractal stability border in plane Couette flow. *Phys. Rev. Lett.* **79**, 5250.

Schneider, T. M., Eckhardt, B. & Yorke, J. 2007 Turbulence, transition, and the edge of chaos in pipe flow. *Phys. Rev. Lett.* **99**, 034502.

Sirovich, L. & Zhou, X. 1994 Reply to 'Observations regarding "Coherence and chaos in a model of turbulent boundary layer" by X. Zhou and L. Sirovich'. *Phys. Fluids* **6**, 1579–1582.

Skufca, J. D. 2005 Understanding the chaotic saddle with focus on a 9-variable model of planar Couette flow. PhD thesis, University of Maryland.

Skufca, J. D., Yorke, J. A. & Eckhardt, B. 2006 Edge of chaos in a parallel shear flow. *Phys. Rev. Lett.* **96**, 174101.

Smith, T. R., Moehlis, J. & Holmes, P. 2005 Low-dimensional models for turbulent plane Couette flow in a minimal flow unit. *J. Fluid Mech.* **538**, 71–110.

Viswanath, D. 2007 Recurrent motions within plane Couette turbulence. *J. Fluid Mech.* **580**, 339–358.

Viswanath, D. 2008 The dynamics of transition to turbulence in plane Couette flow. In *Mathematics and Computation, a Contemporary View. The Abel Symposium* 2006, *Abel Symposia*, vol. 3. Springer.

Waleffe, F. 1995 Hydrodynamic stability and turbulence: beyond transients to a self-sustaining process. *Stud. Appl. Maths* **95**, 319–343.

Waleffe, F. 1997 On a self-sustaining process in shear flows. *Phys. Fluids* **9**, 883–900.

Waleffe, F. 1998 Three-dimensional coherent states in plane shear flows. *Phys. Rev. Lett.* **81**, 4140–4143.

Waleffe, F. 2001 Exact coherent structures in channel flow. *J. Fluid Mech.* **435**, 93–102.

Waleffe, F. 2002 Exact coherent structures and their instabilities: toward a dynamical-system theory of shear turbulence. In *Proc. Int. Symp. on Dynamics and Statistics of Coherent Structures in Turbulence: Roles of Elementary Vortices* (ed. S. Kida), pp. 115–128. National Center of Sciences, Tokyo, Japan.

Waleffe, F. 2003 Homotopy of exact coherent structures in plane shear flows. *Phys. Fluids* **15**, 1517–1543.

Waleffe, F. & Wang, J. 2005 Transition threshold and the self-sustaining process. In *IUTAM Symp. on Laminar–Turbulent Transition and Finite Amplitude Solutions* (ed. T. Mullin & R. R. Kerswell), pp. 85–106. Kluwer.

Wang, J., Gibson, J. F. & Waleffe, F. 2007 Lower branch coherent states in shear flows: transition and control. *Phys. Rev. Lett.* **98** (20), 1–4.

Wedin, H. & Kerswell, R. R. 2004 Exact coherent structures in pipe flow: travelling wave solutions. *J. Fluid Mech.* **508**, 333–371.

Zhou, X. & Sirovich, L. 1992 Coherence and chaos in a model of turbulent boundary layer. *Phys. Fluids* A **4**, 2855–2874.

https://doi.org/10.1017/S002211200800267X Published online by Cambridge University Press